Dynamical mean-field approach to materials with strong electronic correlations

J. Kuneš,[1] I. Leonov,[2] M. Kollar,[2] K. Byczuk,[3] V. I. Anisimov,[4] and D. Vollhardt[2,a]

[1] Institute of Physics, Academy of Sciences of the Czech Republic, Cukrovarnicka 10, Praha 6 16253, Czech Republic
[2] Theoretical Physics III, Center for Electronic Correlations and Magnetism, Institute of Physics, University of Augsburg, 86135 Augsburg, Germany
[3] Institute of Theoretical Physics, University of Warsaw, ul. Hoża 69, 00-681 Warszawa, Poland
[4] Institute of Metal Physics, Russian Academy of Sciences, 620041 Yekaterinburg GSP-170, Russia

Abstract. We review recent results on the properties of materials with correlated electrons obtained within the LDA+DMFT approach, a combination of a conventional band structure approach based on the local density approximation (LDA) and the dynamical mean-field theory (DMFT). The application to four outstanding problems in this field is discussed: (i) we compute the full valence band structure of the charge-transfer insulator NiO by explicitly including the p-d hybridization, (ii) we explain the origin for the simultaneously occuring metal-insulator transition and collapse of the magnetic moment in MnO and Fe_2O_3, (iii) we describe a novel GGA+DMFT scheme in terms of plane-wave pseudopotentials which allows us to compute the orbital order and cooperative Jahn-Teller distortion in $KCuF_3$ and $LaMnO_3$, and (iv) we provide a general explanation for the appearance of kinks in the effective dispersion of correlated electrons in systems with a pronounced three-peak spectral function without having to resort to the coupling of electrons to bosonic excitations. These results provide a considerable progress in the fully microscopic investigations of correlated electron materials.

1 Introduction

The theoretical understanding of materials with strong effective interactions between the electrons is one of the most challenging areas of current research in condensed matter physics [1]. Strong electronic interactions are encountered in materials with open d and f shells, such as the transition metals Ti, V, Fe and their oxides or rare–earth metals such as Ce, where electrons occupy narrow orbitals. This spatial confinement enhances the effect of the Coulomb interaction between the electrons, making them "strongly correlated". The interplay between the spin, charge and orbital degrees of freedom of the correlated d and f electrons and the lattice degrees of freedom leads to a multitude of unusual ordering phenomena at low temperatures. Consequently, strongly correlated electron systems are often exceedingly sensitive to small changes in the temperature, pressure, magnetic field, doping, and other control parameters. This results, for example, in large changes of the resistivity across metal-insulator transitions or upon the application of a magnetic field of the volume across phase transitions, and of the effective electronic masses; electronic correlations are also essential for an understanding of high-temperature superconductivity. Correlated electron materials often reveal rich phase diagrams originating from the interplay between electronic and lattice degrees of freedom [1,2,3]. These compounds

[a] e-mail: `dieter.vollhardt@physik.uni-augsburg.de`

are particularly interesting in view of possible technological applications. Namely, their properties can be employed to construct materials with new functionalities for future technological applications.

The electronic properties of many materials can be computed using density functional theory methods, e.g., in the local density approximation (LDA) [4], the generalized gradient approximation (GGA) [5,6], or using the so-called LDA+U method [7,8,9]. Applications of these approaches often describe the physical properties of simple elements and intermetallic compounds, and of some insulators, quite accurately. Moreover, they permit to make correct qualitative predictions of the magnetic, orbital, and crystal structures of solids where the equilibrium (thermodynamic) structures are determined by simultaneous optimization of the electron and lattice systems [10,11,12,13]. However, these methods usually fail to describe the correct electronic and structural properties of electronically correlated *paramagnetic* materials. Hence the computation of electronic, magnetic, and structural properties of strongly correlated paramagnetic materials remains a great challenge.

Here the recent combination of conventional band structure theory [4] and dynamical mean-field theory [14,15,16,17,18], the so-called LDA+DMFT computational scheme [19,20,21,22,23,24] has led to a powerful new tool for the investigation of strongly correlated compounds both in their paramagnetic and magnetically ordered states. In particular, it has already provided important insights into the spectral and magnetic properties of correlated electron materials [25,26,27,28,29,30,31,32,33,34,35,36,37,38,39,40,41,42,43,44] especially in the vicinity of a Mott metal-insulator transition as encountered in transition metal oxides.

In this paper we review several topics related to the physics of correlated electron materials where significant progress was made during the last three to four years. In particular we describe the application of the LDA+DMFT approach to charge-transfer materials where — in contrast to the early transition metal oxides — additional complexities from the presence of p bands arise. We apply the scheme to study the single-particle spectrum of the prototypical charge-transfer insulator NiO. By explicitly including the O-p orbitals and their hybridization with Ni-d orbitals we obtain a unified description of the full spectrum (Sec. 2). A second topic is the investigation of the influence of pressure on correlated electronic materials and of the collapse of the magnetic moment. Indeed, in numerous transition-metal oxides the pressure-induced metal-insulator transition is accompanied by a collapse of the magnetic moments, i.e., a transition from a high spin state to a state with low spin. Such a transition is observed for example in MnO and Fe_2O_3. Our results obtained with LDA+DMFT for MnO are described in Sec. 3. A breakthrough in the application of the LDA+DMFT scheme concerning the computation of correlation induced atomic displacements and structural transformations is presented in Sec. 4. Namely, by formulating a LDA/GGA+DMFT scheme implemented with plane-wave pseudopotentials it has been possible to describe and understand the structural transformation of paramagnetic solids due to electronic correlation effects. Finally, we present a general explanation for the appearance of kinks, i.e., sudden changes in the slope of the effective electronic dispersion of the correlated electrons. By a detailed analytic investigation of the Green function and the self-energy for correlated systems with a pronounced three-peak spectral function we are able to explain the occurrence of kinks without having to resort to any explicit coupling of electrons to bosonic excitations (Sec. 5).

2 Charge-transfer compounds

In the so-called charge-transfer (CT) materials the ligand orbitals play an important role since they determine the low-energy physics of these systems. The concept of a CT insulator was introduced in the mid 1980's by Zaanen, Sawatzky and Allen (ZSA) in their classification of transition-metal oxides (TMOs) and related compounds [45]. In the early TMOs the ligand p band is located well below the transition metal d band and thus plays a minor role in the low energy dynamics. Such a case, called Mott-Hubbard system in the ZSA scheme, is well described by a multi-band Hubbard model. On the other hand, the late TMOs are of the CT type where the p band is located between the interaction split d band. A more general

Hamiltonian where the p states are explicitly included is then needed, which can be viewed as a combination of multi-band Hubbard and Anderson lattice models. The results of calculations using the static mean-field approximation such as LDA+U [7,8,9] suggested that the treatment of the dynamical correlations and the ligand–transition-metal hybridization might be important to properly describe the excitations in the CT materials.

NiO is a well-studied prototype of a CT insulator. It is a type II anti-ferromagnet (T_N = 523 K) with a magnetic moment of almost $2\mu_B$ and a large gap surviving well above T_N. Its photoemission spectrum [46,47,48,49], which is our main concern, has several characteristic features: (i) a broad high-energy peak with little dispersion dominated by Ni d character, (ii) a flat low-energy band with substantial amount of Ni d character, (iii) dispersive O p bands at intermediate energies, and (iv) a charge gap of 3-4 eV. All of these feature are essentially the same in both the antiferro- and the paramagnetic phase [50]. Although further details can be resolved in the spectra of NiO we will focus on these four features here.

The LDA+DMFT calculations proceeds in two independent steps: the construction of the effective Hamiltonian from converged LDA calculation, and the subsequent solution of the corresponding DMFT equations. We use the Wannier function basis [51,52] for an eight-band p-d Hamiltonian

$$H = \sum_{\boldsymbol{k},\sigma} \left(h^{dd}_{\boldsymbol{k},\alpha\beta} d^\dagger_{\boldsymbol{k}\alpha\sigma} d_{\boldsymbol{k}\beta\sigma} + h^{pp}_{\boldsymbol{k},\gamma\delta} p^\dagger_{\boldsymbol{k}\gamma\sigma} p_{\boldsymbol{k}\delta\sigma} + h^{dp}_{\boldsymbol{k},\alpha\gamma} d^\dagger_{\boldsymbol{k}\alpha\sigma} p_{\boldsymbol{k}\gamma\sigma} + h^{pd}_{\boldsymbol{k},\gamma\alpha} p^\dagger_{\boldsymbol{k}\gamma\sigma} d_{\boldsymbol{k}\alpha\sigma} \right)$$
$$+ \sum_{i,\sigma,\sigma'} U^{\sigma\sigma'}_{\alpha\beta} n^d_{i\alpha\sigma} n^d_{i\beta\sigma'}. \tag{1}$$

Here $d_{\boldsymbol{k}\alpha\sigma}$ and $p_{\boldsymbol{k}\gamma\sigma}$ are Fourier transforms of $d_{i\alpha\sigma}$ and $p_{i\gamma\sigma}$, which annihilate the d or p electron with orbital and spin indices $\alpha\sigma$ or $\gamma\sigma$ in the ith unit cell, and $n^d_{i\alpha\sigma}$ is the corresponding occupation number operator. The elements of the $U^{\sigma\sigma'}_{\alpha\beta}$ matrix are parameterized by U and J. The constrained LDA calculation yields $U = 8$ eV and $J = 1$ eV [7]. To account for the Coulomb energy already present in LDA we subtract a double counting correction from the dd-diagonal elements of the LDA Hamiltonian:

$$h^{dd}_{\boldsymbol{k},\alpha\beta} = \tilde{h}^{dd}_{\boldsymbol{k},\alpha\beta}(\boldsymbol{k}) - (N_{\mathrm{orb}} - 1)\bar{U} n_{\mathrm{LDA}} \delta_{\alpha\beta} \tag{2}$$

where n_{LDA} is the average LDA occupation per orbital and $N_{\mathrm{orb}} = 10$ is the total number of orbitals within the shell. With the kinetic and interaction parts of the Hamiltonian specified we solve the DMFT equations on the imaginary frequency axis, a key part of which is the auxiliary impurity problem treated with the quantum Monte-Carlo (QMC) method [53]. The results reported here were calculated at $T = 1160$ K. To obtain the single-particle spectral functions an analytic continuation to real frequencies is performed using the maximum entropy method [54].

We start the discussion of our numerical results with the single-particle spectra of stoichiometric NiO. Using the full p-d Hamiltonian we are able to cover the entire valence and conduction bands spectra. In the left panel of Fig. 1 we show the local ($\boldsymbol{k}$-integrated) spectral densities corresponding to Ni d e_g and t_{2g}, as well as O p electrons. In the inset we compare the total Ni d spectral density to the experimental data of Sawatzky and Allen [46]. The theoretical spectrum very well reproduces the experimental one, including the size of the gap, the d character of the conduction band, the broad d peak at -9 eV, the position of the p band, and the strong d contribution at the top of the valence band. The dominant feature of the valence spectrum is a distribution of spectral weight between the broad peak at high energy and sharp peaks at low energy. The spectral weight distribution is a combined effect of the p-d hybridization and the electronic correlation in the Ni d shell as was explained by Fujimori *et al.* [55] in terms of eigenstates of a NiO$_6$ cluster, and Sawatzky and Allen [46]. Emitting a d electron from the d^8 state the system can reach either the d^7 final state (high-energy peak) or a $d^8\underline{L}$ final state (sharp low-energy peak), with a ligand hole, due to the p-d electron transfer.

Virtually all electronic structure computational methods have been applied to NiO, often claiming success in describing its photoemission spectrum. However, these claims are often
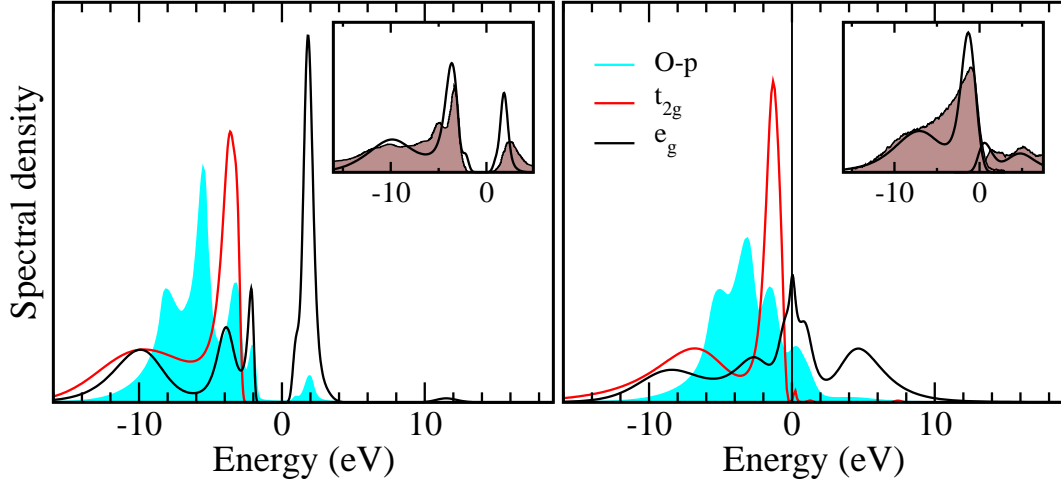
Fig. 1. (color online) Left panel: the orbitally resolved single-particle spectrum of NiO with contributions from Ni d-e_g (black), Ni d-t_{2g} (red), and O p (blue shaded) states. The inset shows comparison of the total Ni d spectral density (with Gaussian broadening of 0.6 eV) (black) to the XPS spectra (brown shaded) of Ref. [46]. Right panel: the orbitally resolved single-particle spectrum of hole doped NiO ($n_h = 0.6$). The total Ni d spectrum (black) is compared to the experimental photoemission and inverse-photoemission spectra of $Li_{0.4}Ni_{0.6}O$ [56] (brown shaded).

based on picking only a particular aspect of the problem. Putting aside the fact that static methods such as LDA+U [7,8,9] and generalized density functionals [5,6] as well as GW [57,58] provide gapped spectra only in the AFM phase, the main difficulty appears to be capturing the distribution of spectral weight between the high-energy d^7 peak of Ni d character and the low-energy $d^8\underline{L}$ band with mixed Ni d - O p composition. For example, the high-energy Ni d peak is completely missing in the calculations with the recently introduced density [5,6] and density matrix [59] functionals and also in GW calculations [57,58,60,61] for reasons explained in Ref. [62]. Also LDA+U calculations with small U miss the high-energy peak [63]. On the other hand, for larger U values the d character is missing in the low-energy peak [7,61]. The early LDA+DMFT calculations of Ren *et al.* [64] also do not yield qualitatively correct valence band since the O p states were not included in the effective Hamiltonian. On the other hand many-body techniques such as cluster exact diagonalization [55], three-body scattering technique [65] or DMFT [41,42,66,67,68], which are capable of generating new poles in the single-particle self-energy, describe the distribution of the valence spectral weight in agreement with experiment.

To further investigate the electronic structure of NiO we have calculated the $\boldsymbol{k}$-resolved spectra, which determine the correlated bandstructure. In Fig. 2 we compare the theoretical bands, represented by the $\boldsymbol{k}$-dependent spectral density $A(\boldsymbol{k}, \omega)$, along the $X - \Gamma$ and $\Gamma - K$ lines in the Brillouin zone with ARPES data of Refs. [48,49]. Both theory and experiment exhibit two relatively flat bands at -2 and -4 eV followed by several dispersive bands in the -4 to -8 eV range and a broad incoherent peak around -10 eV. Overall we find a good agreement. The deviations around the Γ point in the right panel of Fig. 2 are due to the inaccuracy in the location of the Γ point in the off-normal-emission experiment [49]. The crosses near the Γ point mark a weak band which was interpreted as a consequence of AFM order [49] and is therefore not expected to be found in the paramagnetic phase investigated here. Additional weak structures in the uppermost valence band (not shown here) were identified in the spectra of Ref. [49]. To assess their importance the reader is referred to the original experimental spectra.

The effect of doping holes to a CT insulator is of prime importance, particularly because the high-temperature superconductivity is widely believed to arise from this effect. Besides that, the p character of the doped holes is a defining feature of CT materials. In NiO hole doping can be achieved by Li substitution. $Li_xNi_{1-x}O$ was studied in the doping range $x = 0.02$-0.4 [56].
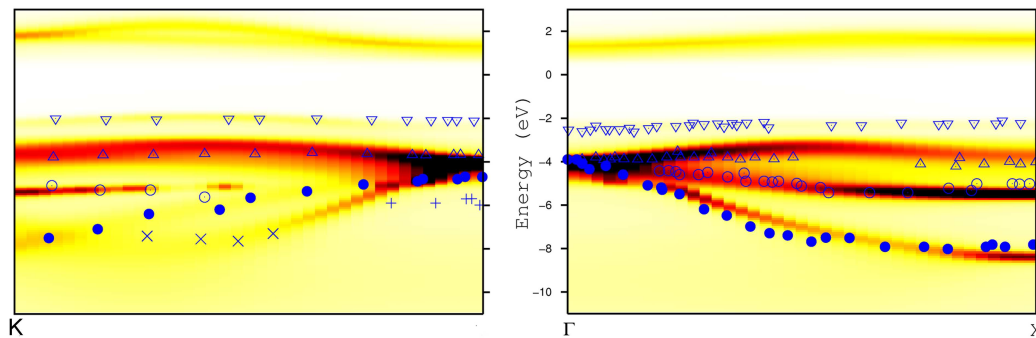
Fig. 2. The $\boldsymbol{k}$-resolved total spectral function $A(\boldsymbol{k},\omega)$ along the $K - \Gamma$ (left panel) and $\Gamma - X$ (right panel) lines in the Brillouin zone depicted as a contour plot. The symbols represent the experimental bands of Shen *et al.* [49]. The theoretical gap edge was aligned with the experimental one.

Table 1. Orbital occupancies and the local moment on the Ni site for different hole dopings.

n_h	n_{e_g}	$n_{t_{2g}}$	n_p	M_s	M_{eff}
0	0.547	1.000	0.969	1.85	1.82
0.6	0.531	0.994	0.885	1.61	1.27
1.2	0.530	0.980	0.800	1.45	0.89

Starting from the undoped system the replacement of x Ni^{2+} ions by Li^{1+} ions introduces on average $n_h = x/(1 - x)$ holes per Ni site. In the following, we neglect the substitutional disorder and study the Hamiltonian of NiO at various non-stoichiometric fillings. As crude as this approximation may be we believe that the essential physics of p-d spectral weight transfer is captured correctly. In Table 1 we compare the orbital occupancies and local spin moment for different hole dopings. While a substantial d spectral density is observed at the top of NiO valence band the doped holes reside almost exclusively in oxygen p orbitals. This apparent contradiction to the experience from non-interacting electron systems reflects the importance of many-body effects.

Yet another demonstration of electronic correlations is a substantial reconstruction of the spectral function, in particular the e_g one, shown in the left panel of Fig. 1. Most notably the Mott gap is filled, while the Hubbard subbands remain as distinct features with the spectral weight reduced as compared to pure NiO. This is also observed in experiment, as shown in the inset. To understand the spectrum it is useful to think about the doping in two steps. First, the holes are doped into a system with no p-d hybridization. For the present heavy doping this simply amounts to shifting the chemical potential deep into the non-interacting p band. Second, the p-d hybridization is turned on and the system is essentially described by the periodic Anderson model with a well known spectrum similar to that for the e_g orbital [69].

While the d occupancy is barely affected by the hole doping, the behavior of the local spin moment changes. The instantaneous moment $M_s = \sqrt{\langle \hat{m}_z^2 \rangle}$ is reduced due to the suppression of the dominant d^8, $m_z = 2$ contributions in favor of d^6, d^7, and d^8 contributions with $m_z = 0$ and $m_z = 1$. Even more pronounced is the effect of increased screening of the local moment, reflected in faster decay of imaginary time spin-spin correlations (see Fig. 3), leading to a significant departure of the screened moment $M_{\text{eff}} = \sqrt{T\chi_{\text{loc}}}$ from its instantaneous value.

To summarize, we have presented LDA+DMFT calculations on NiO and its hole doped relatives using a Hamiltonian spanning Ni $3d$ and O $2p$ bands. It appears that the main limitation of the truly first principles character of LDA+DMFT studies is the need for a double-counting correction, the universal form of which is not known, and perhaps does not exist. We also mention the density-density form of the electron-electron interaction used here, a rather technical approximation, which can be avoided with the most recent CT-QMC implementations [71] or exact diagonalization [70]. Despite these approximations we were able to obtain the main
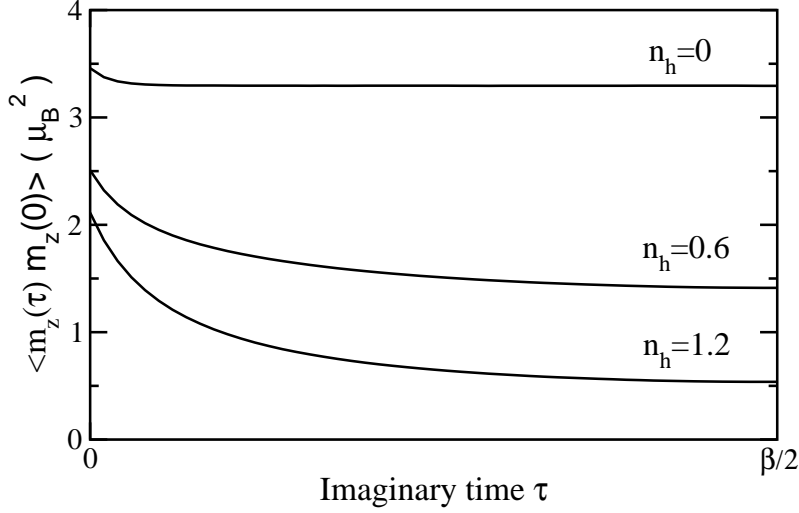
Fig. 3. The imaginary time spin-spin correlations $\langle m_z(\tau) m_z(0) \rangle$ for various hole dopings. The calculations were performed at 1160 K ($\beta = 10 \text{ eV}^{-1}$).

characteristics of the photoemission and inverse-photoemission spectra of both pure and hole-doped NiO. The computational methods claiming success for NiO and CT compounds in general should be able to capture substantial d spectral weight at the top of the valence band together with the incoherent lower Hubbard band, and, perhaps most importantly, should be able to describe the peculiar behavior upon hole doping.

3 Metal-insulator and spin transitions

A very interesting type of metal-insulator transition (MIT) is the pressure driven transition accompanied by a change of the local spin state (high spin (HS) to low spin (LS) transition) seen in MnO [72], BiFeO$_3$ [73] or Fe$_2$O$_3$. An understanding of the pressure-driven HS-LS transition and its relationship to the MIT and to structural and/or volume changes is relevant to a broader class of oxides [74], often with geophysical implications [75].

We have studied two isoelectronic materials which exhibit the above behavior under pressure, hematite (α-Fe$_2$O$_3$) [44] and manganosite (MnO) [43]. At ambient conditions, Fe$_2$O$_3$ is an antiferromagnetic (AFM) insulator ($T_N = 956$ K) with the corundum structure [76] while MnO is antiferromagnetic only below 118 K and possesses rock-salt structure. In both compounds the transition metal (TM) ions have formal valence state d^5 and are octahedrally coordinated with oxygen, which gives rise to the characteristic e_g-t_{2g} splitting. Photoemission spectroscopy (PES) at zero pressure [77,78,79] classified Fe$_2$O$_3$ as a charge-transfer insulator with the charge gap of 2.0-2.7 eV inferred from the electrical conductivity data [80,81]. Under pressure, a first-order phase transition is observed at approximately 50 GPa (82% of the equilibrium volume) with the specific volume decreasing by almost 10% and the crystal symmetry being reduced (to the Rh$_2$O$_3$-II structure) [82,83,84]. The high-pressure phase is characterized by a metallic conductivity and the absence of both magnetic long-range order and the HS local moment [82]. Badro *et al.* showed that the structural transition actually precedes the electronic transition, which is, nevertheless, accompanied by a sizable reduction of the bond lengths [85].

MnO shows a similar behavior. The shock data [86], and then Raman and optical studies [87,88], had identified a transformation in MnO in the vicinity of 90-105 GPa. Transport [89], magnetic [89], structural and spectroscopic [90,91], and reflectivity [87] data all point to a first-order, insulator-metal Mott transition near 100 GPa with volume ($v = V/V_0$, $V_0 =$ volume at ambient pressure) collapse $v = 0.68 \rightarrow 0.63$, and moment collapse (from $\sim 5\mu_B$ to $1\mu_B$ or
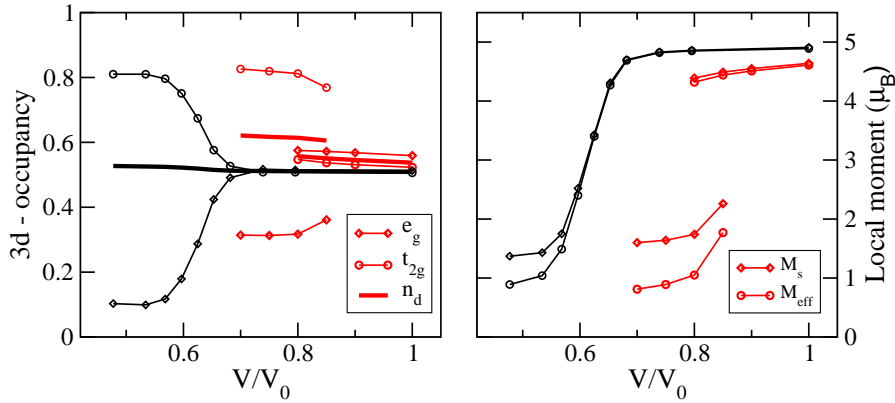
Fig. 4. Left panel: the orbital-resolved occupancies of the $3d$ shell of Fe in Fe_2O_3 (red) and Mn in MnO (black). The thick lines show the average occupancy n_d per orbital. Right panel: the local spin moments in Fe_2O_3 (red) and MnO (black) measured as instantaneous moment (diamonds) and screened moment (circles). The symbols mark the actual numerical results, the lines are guides to the eye. V_0 is the volume at ambient pressure. Adapted from [43].

less [90,91]). The structural data indicate a B1→B8 change just before the Mott transition, which thus occurs within the B8 (NiAs) phase rather than the B1 (NaCl) phase. Since the local environment of the Mn ion remains the same, this structural change is not expected to have much effect on the Mott transition.

Our calculations proceed along the lines described in the preceding section: i) construction of the multi-band Hubbard Hamiltonian spanning the TM d and ligand p bands with local Coulomb interaction within the TM d shell in the density-density (Ising) approximation, ii) iterative solution of the DMFT equations on the imaginary axis using QMC, iii) computation of observables of interest. This procedure has been repeated for several lattice parameters corresponding to pressures up to several 100 GPa. In the case of MnO we employed the Hirsch-Fye QMC algorithm available at the time, for which the calculations were limited to the temperature $T = 1160$ K. For the Fe_2O_3 study the continuous-time QMC algorithm (hybridization expansion) was used, which allowed us to reach room temperature and study the anti-ferromagnetic ordering. In both cases we had to introduce special Monte-Carlo moves to ensure ergodic simulation for parameters close to the spin transition. The calculated observables include the single-particle spectral density to study the formation of the charge gap, local orbital occupancies $\langle n_i \rangle$ and static local density-density correlations $\langle n_i n_j \rangle$ to investigate the orbital redistributions, instantaneous local moments and interaction energy, and local spin susceptibility to determine the screening of the local spin moments.

In Fig. 4 we show the evolution of the local moments and the orbital occupancies as functions of specific volume. We use two different quantities to characterize the local moment: (a) the mean instantaneous moment defined as an equal time correlation function $M_s = \sqrt{\langle \hat{m}_z^2 \rangle}$ and (b) the screened local moment defined through the local spin susceptibility $M_{\text{eff}} = \sqrt{T \chi_{\text{loc}}}$. These two different definitions of the local moment yield almost the same T-independent values in materials with Curie-Weiss behavior. The two studied materials exhibit clear similarities. In particular, the HS state with $M_s \sim 5$ and orbital occupancies corresponding to the complete spin polarization of a half-filled d shell dictated by the first Hund's rule, the LS state characterized by emptying of the e_g orbitals, substantial reduction of the local moment and the screening of the local moment reflected in the difference between M_s and M_{eff}. Furthermore it turns out that the charge gap disappears in the LS phase (see Figs. 5 and 6).

Nevertheless, there are also several differences between MnO and Fe_2O_3. Their orbital occupancies differ quantitatively, especially the e_g occupancies in the LS phase are substantially larger in Fe_2O_3. This is a result of more covalent character of this compound, i.e., stronger p-e_g mixing. Another consequence of the strong covalent p-e_g bonding is a transfer of charge
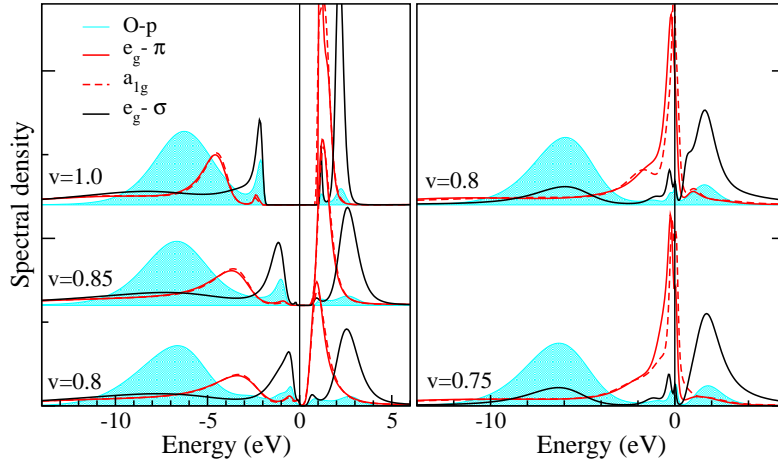
Fig. 5. The single-particle spectra of Fe_2O_3 at various specific volumes ($T = 580$ K) [44]. The HS solutions are shown in the left and LS solutions in the right panel. The Fe d spectra are resolved into the e_g (called e_g^σ in the legend) and t_{2g} (further split in a_{1g} and e_g^π by distortion from precise octahedral symmetry) contributions. The O p spectra are marked by blue shading.
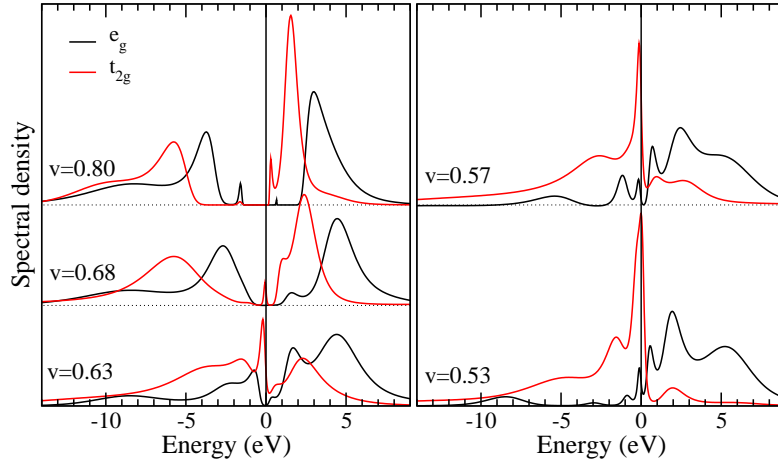

Fig. 6. The single-particle spectra of MnO at various specific volumes ($T = 1160$ K) in the vicinity of the spin transition [43]. The Mn d spectra are resolved into the e_g and t_{2g} contributions, O p spectra are not shown.

between Fe and O upon the HS-LS transition, reflected in the difference of the total occupancies n_d in the two phases. There is also a qualitative difference between the transitions in MnO and Fe_2O_3. In MnO we find a smooth crossover characterized by a unique solution for all specific volumes with intermediate magnetic moments, and only when the lattice is included we observe a phase separation into high-volume HS phase and low-volume LS phase in the crossover region. In Fe_2O_3 we observe an electronically first-order transition with hysteresis.

Next, we compare the evolution of the single-particle spectral densities (see Figs. 5 and 6) as the volume is reduced. In both cases we observe the closing of the HS charge gap as the material is compressed, and LS spectra that bear clear resemblance to the non-interacting bands with some quasiparticle renormalization. However, there is a clear difference in the way the HS gap disappears. In Fe_2O_3 (Fig. 5) the gap can be squeezed arbitrarily small without qualitative changes of the spectra and the HS phase becomes unstable only when the gap is zero (within the numerical accuracy and resolution). In contrast, the transition in MnO does not proceed by
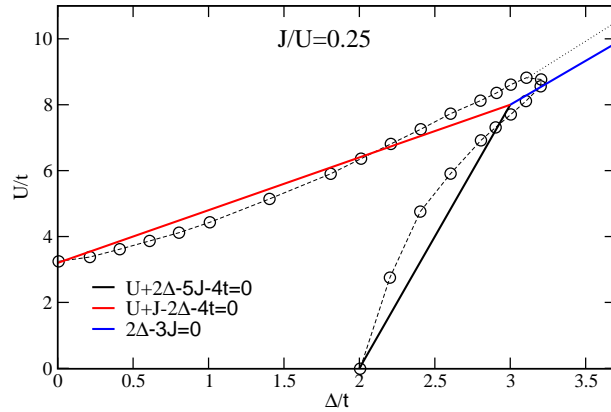
Fig. 7. Comparison of the phase boundaries of the two-band obtained with full DMFT (QMC) calculation (taken from Ref. [92]) with the phase boundaries obtained by simple ionic estimates described in the text. The boundary between the "metal" and "band insulator" was obtained by setting the charge gap above the band insulator ground state to zero.

squeezing the gap to zero, but by appearance of in-gap states. We use this observation below to discuss how the d^5 HS phase is destabilized.

For the sake of clarity we simplify the local interaction to $\sum_{i,j,\sigma} U n_{i\sigma} n_{j-\sigma} + (U-J) n_{i\sigma} n_{j\sigma}$ in the following discussion. We will estimate two quantities, the charge gap in the HS phase:

$$E_{\mathrm{g}} \approx E(d^6) + E(d^4) - 2E(d^5) - W = U + 4J - \Delta - W, \qquad (3)$$

and the difference (per atom) between the LS and HS ground states:

$$E(\mathrm{LS}) - E(\mathrm{HS}) = 6J - 2\Delta. \qquad (4)$$

Here Δ is the e_g-t_{2g} crystal-field splitting, W is an effective bandwidth, which describes reduction of the ionic gap due to the actual bandwidth and the charge-transfer parameter, $E(d^5)$ is the ground-state energy of an ion in the HS state and $E(d^6)$, $E(d^4)$ are the energies of the corresponding electron addition and removal states, respectively. The estimates are obtained by simple ionic considerations. The interaction parameters U and J are considered to remain constant, while the crystal-field splitting Δ and the bandwidth W increase with pressure. The insulating HS state is destabilized when either (3) or (4) becomes zero. Which of the two quantities reaches zero first depends on the parameters of the system. We have adopted the terms *gap closing* and *local state transition* for the former and the latter instability, respectively.

Comparing the behavior of the charge gap in Fe_2O_3, where the HS phase exists as long as the gap is finite, and in MnO, where the transition starts while the gap is still finite, leads to the conclusion that the observed metal-insulator transition in Fe_2O_3 proceeds by the gap closing while in MnO the local state transition takes place. Interestingly, a similar behavior was observed in the two-band model studied by Werner and Millis [92]. In Fig. 7 we put the transition lines obtained from approximate expressions like (3) and (4) adapted for the two-band model on top of the numerical results obtained by the DMFT solution of the two-band model. Thus we can identify the transition between the "Mott insulator" and the "metal", in the language of Ref. [92], with the gap closing and the transition between "Mott insulator" and the "band insulator" with the local state transition. Note that the third transition (black line) exists in the two-band model with two electrons, but not in a five-band model with five electrons relevant for the studied materials. The example of the two-band model shows that the gap closing and local state transition concepts are quite general. Similar ionic considerations were recently used by Lyubutin *et al.* [74] to other fillings of the d shell. It was also shown that for d^5 Eq. 3 holds only if $\Delta < 2J$.

In studying the relationship between metal-insulator and spin transitions in Fe_2O_3 and MnO we discussed two scenarios how an insulating HS phase can be destabilized. In the first

one, the charge gap is closed due to increase of the crystal field as well as the bandwidths so that the system becomes metallic, at which point the ionic reasoning presented here and in Ref. [74] breaks down. In the second one, the local HS becomes energetically unfavorable while the charge gap is still finite and the system transforms into a LS phase, which may be either metallic or insulating, e.g., LuFeO$_3$ [93,94], depending on the parameters of the system.

4 Correlation-induced atomic displacements and structural transformations

Previous applications of the LDA+DMFT approach have focused on the investigation of correlation effects in the electronic system with a given lattice structure, thereby neglecting the mutual interaction between electrons and ions. As a result, the influence of the electrons on the lattice structure was disregarded. Recent applications of LDA+DMFT, e.g., computations of the volume collapse in paramagnetic Ce [30,31,32] and Pu [33,34,35] and of the collapse of the magnetic moment in MnO [43], did include the lattice, but only calculated the total energy of the correlated material as a function of the unit cell volume [95]. Moreover, these implementations of LDA+DMFT cannot describe the electronic and structural properties of electronically correlated materials in the case of structural transformations, e.g., involving the cooperative Jahn-Teller (JT) effect [96,97,98,99,100]. This is due to the atomic-sphere approximation within the linearized and higher-order muffin-tin orbital [L(N)MTO] techniques [101,102] which are conventionally used in the LDA+DMFT approach. The approximation employs a spherical potential inside the atomic sphere, thereby neglecting multipole contributions to the electrostatic energy due to the distorted charge-density distribution. This makes the L(N)MTO technique unsuitable to determine atomic positions reliably. Instead, the recently proposed implementation of the LDA+DMFT approach [103,104,105,106,107,108], which employs plane-wave pseudopotentials [10,11] and thus avoids the atomic sphere approximation, does not neglect such contributions. Thereby it becomes possible to describe the effect of the distortion on the electrostatic energy [103,104].

Here we discuss the LDA+DMFT scheme implemented with plane-wave pseudopotentials [103,104,105] to compute structural transformations, e.g., structural phase stability and structure optimization, caused by electronic correlations. Most importantly, this scheme is able to determine correlation-induced structural transformations in both paramagnetic and long-range ordered solids. Thereby it is able to overcome the limitations of standard band-structure approaches and earlier implementations of the LDA+DMFT approach, and opens the way for fully microscopic investigations of the structural properties of strongly correlated electron materials. In the following we present the application of this approach to the investigation of orbital order and the cooperative JT distortion in two prototypical JT materials, KCuF$_3$ and LaMnO$_3$, and compute the electronic, structural, and orbital properties in their room-temperature paramagnetic phase. These are the first results obtained for a structural optimization where the stability of the cooperative JT distortion in paramagnetic KCuF$_3$ and LaMnO$_3$ is investigated using total energy calculations [109].

4.1 Application to KCuF$_3$

KCuF$_3$ is a prototype material regarding the cooperative Jahn-Teller (JT) effect, orbital ordering, and low-dimensional magnetism [97,98,99,100,110]. It is an insulating pseudocubic perovskite whose structure is related to that of high-temperature superconductors and colossal magnetoresistance manganites. The copper ions have octahedral fluorine surrounding and are nominally in a Cu^{2+} ($3d^9$) electronic configuration, with completely filled t_{2g} orbitals and a single hole in the e_g states. This gives rise to a strong JT instability that lifts the cubic degeneracy of the Cu e_g states due to a cooperative JT distortion [97,98,99,100]. The latter is characterized by CuF$_6$ octahedra elongated along the a and b axis and arranged in an antiferro-distortive pattern in the ab plane [111]. The strong JT distortion persists up to the melting temperature (~ 1000 K) and is associated with the particular orbital order in KCuF$_3$, in which a single hole alternatingly occupies $d_{x^2-z^2}$ and $d_{y^2-z^2}$ orbital states, resulting in a tetragonal compression

($c < a$) of the unit cell. Purely electronic effects as in the Kugel-Khomskii theory [97,98,99,100] and the electron-lattice [112] interaction have been discussed as a possible mechanism behind the orbital ordering in KCuF$_3$. Nevertheless, the mechanism responsible for the orbital order in KCuF$_3$ is still being debated in the literature [8,97,98,99,100,103,112,113,114,115].

KCuF$_3$ has a relatively high (tetragonal, space group $I4/mcm$) crystal symmetry, hence it is one of the simplest systems to study. The JT distortion in KCuF$_3$ can be expressed using a single internal structure parameter, the shift of the in-plane fluorine atom from the Cu-Cu bond center. Moreover, KCuF$_3$ has a single hole in the $3d$ shell resulting in the absence of multiplet effects. The electronic and structural properties of KCuF$_3$ have been intensively studied by density functional theory in the local density approximation (LDA) [4], the generalized gradient approximation (GGA) [5,6,116], or using the so-called LDA+U approach [7,8,9]. While the LDA+U calculations account rather well for the value of the equilibrium JT distortion in KCuF$_3$ [115], the calculations simultaneously predict a long-range antiferromagnetic order which indeed occurs in KCuF$_3$ below $T_N \sim 22$–38 K [117]. The LDA+U calculations give the correct insulating ground state with the long-range A-type antiferromagnetic and $d_{x^2-z^2}/d_{y^2-z^2}$ antiferro-orbital order [8,113,115], consistent with the Goodenough-Kanamori-Anderson rules for a superexchange interaction. Moreover, LDA+U calculations for a model structure of KCuF$_3$ in which cooperative JT distortions are completely neglected reproduce the correct orbital order, suggesting an electronic origin of the ordering [8,113] in agreement with the Kugel-Khomskii theory [97,98,99,100]. Nonmagnetic LDA/GGA calculations instead predict a *metallic* behavior and cannot explain the insulating paramagnetic behavior at $T > T_N$. The electronic and structural properties of KCuF$_3$ have been recently reexamined by means of LDA+U molecular-dynamic simulations, indicating a possible symmetry change and challenging the original assignment of tetragonal symmetry [115]. This symmetry change seems to allow for a better understanding of Raman [118], electronic paramagnetic resonance [119,120,121], and x-ray resonant scattering [122,123] properties at $T \approx T_N$. However, the details of this distortion have not been fully understood yet. While the LDA+U approach is able to determine electronic properties and the JT distortion in KCuF$_3$ rather well [115], its application is limited to temperatures below T_N. Therefore LDA+U cannot explain the properties at $T > T_N$ and, in particular, at room temperature, where KCuF$_3$ is a correlated paramagnetic insulator with a robust JT distortion which persists up to the melting temperature. To determine the correct orbital order and cooperative JT distortion for a correlated paramagnet, i.e., to perform a structural optimization, we here employ the novel GGA+DMFT scheme implemented with plane-wave pseudopotentials [103,104,105].

We start by calculating the nonmagnetic GGA band structure of KCuF$_3$ within the plane-wave pseudopotential approach [124]. In this calculation we use the Perdew-Burke-Ernzerhof exchange-correlation functional together with Vanderbilt ultrasoft pseudopotentials for copper and fluorine, and a soft Troullier-Martin pseudopotential for potassium. The calculation was performed for the experimental room-temperature crystal structure with space group $I4/mcm$ and lattice constants $a = 5.855$ and $c = 7.852$ Å [111]. We have used different values of the JT distortion δ_{JT} defined accordingly as $\delta_{JT} = \frac{1}{2}(d_l - d_s)/(d_l + d_s)$; d_l and d_s denote the long and short Cu-F bond distances in the ab plane of CuF$_6$ octahedra, respectively, and $2(d_l + d_s) = a$. We express the distortion δ_{JT} in percent of the lattice constant a, e.g., $\delta_{JT} = 0.002 \equiv 0.2\%$, and consider $0.2\% \leq \delta_{JT} \leq 7\%$. The structural data [111] at room-temperature yield $\delta_{JT} = 4.4\%$. In the present calculation we keep the lattice parameters a and c and the space group symmetry fixed.

For all values of δ_{JT} considered here, the nonmagnetic GGA calculations yield a *metallic* rather than the experimentally observed insulating behavior. We also find an appreciable orbital polarization due to the crystal field splitting. Overall, the GGA results qualitatively agree with previous band-structure calculations [8,115]. Thus, the electron-lattice interaction alone is found insufficient to stabilize the orbitally ordered insulating state. The GGA total energy profile is seen to be almost constant for $\delta_{JT} < 4\%$, with a very shallow minimum at about 2.6%. (see Fig. 8, left panel). This would imply that KCuF$_3$ has no JT distortion for temperatures above 100 K, which is in clear contradiction to experiment. Obviously, a JT distortion by itself,
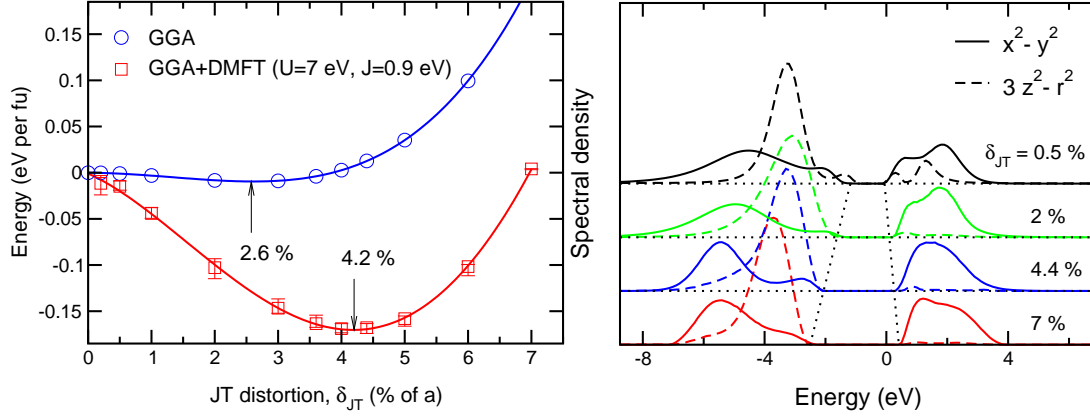
Fig. 8. Left panel: Comparison of the total energies of paramagnetic $KCuF_3$ computed by GGA and GGA+DMFT (QMC) as a function of the JT distortion [103,104]. Error bars indicate the statistical error of the DMFT(QMC) calculations. Right panel: Orbitally resolved Cu e_g spectral densities of paramagnetic $KCuF_3$ as obtained by GGA+DMFT(QMC) for different values of the JT distortion. The resulting orbitally resolved spectral density which is shown here by solid [dashed] line is predominantly of $x^2 - y^2$ [$3z^2 - r^2$] character (in the local frame [125]).

without the inclusion of electronic correlations in the paramagnetic phase, cannot explain the experimentally observed orbitally ordered *insulating* state of $KCuF_3$.

The next step is the construction of an effective low-energy Hamiltonian $\hat{H}_{GGA}$ for the correlated, partially filled Cu e_g orbitals for each value of the distortion δ_{JT} considered here. This is achieved by employing the pseudopotential plane-wave GGA results and making a projection onto atomic-centered symmetry-constrained Cu e_g Wannier orbitals [51,52,105]. Taking the local Coulomb repulsion $U = 7$ eV and Hund's rule exchange $J = 0.9$ eV into account, we obtain the following low-energy Hamiltonian for the two ($m = 1, 2$) Cu e_g bands:

$$\hat{H} = \hat{H}_{GGA} + U \sum_{im} \hat{n}_{im\uparrow}\hat{n}_{im\downarrow} + \sum_{i\sigma\sigma'}(V - \delta_{\sigma\sigma'}J)\hat{n}_{i1\sigma}\hat{n}_{i2\sigma'} - \hat{H}_{DC}. \quad (5)$$

Here the second and third terms on the right-hand side describe the local Coulomb interaction between Cu e_g electrons in the same and in different orbitals, respectively, with $V = U - 2J$, and $\hat{H}_{DC}$ is a double counting correction which accounts for the electronic interactions already described by the GGA (see below). We solve the many-body Hamiltonian (5) for each value of δ_{JT} using the single-site DMFT with Hirsch-Fye quantum Monte Carlo (QMC) calculations [53,126]. The calculations were performed at $T = 1160$ K ($\beta = 10$ eV^{-1}), using 40 imaginary-time slices [127]. For all values of δ_{JT} considered here, we compute the GGA+DMFT total energy as [32,103,104]

$$E = E_{GGA}[\rho] + \langle \hat{H}_{GGA} \rangle - \sum_{m,k} \epsilon_{m,k}^{GGA} + \langle \hat{H}_U \rangle - E_{DC}, \quad (6)$$

where $E_{GGA}[\rho]$ is the total energy obtained by GGA. The third term on the right-hand side of Eq. (6) is the sum of the GGA Cu e_g valence-state eigenvalues and is given by the thermal average of the GGA Hamiltonian with the GGA Green function $G_{\boldsymbol{k}}^{GGA}(i\omega_n)$:

$$\sum_{m,k} \epsilon_{m,k}^{GGA} = \frac{1}{\beta} \sum_{n,\boldsymbol{k}} \text{Tr}[H_{GGA}(\boldsymbol{k})G_{\boldsymbol{k}}^{GGA}(i\omega_n)]e^{i\omega_n 0^+}. \quad (7)$$

The average $\langle \hat{H}_{GGA} \rangle$ is evaluated similarly but with the full Green function including the self-energy. The interaction energy $\langle \hat{H}_U \rangle$ is computed from the double occupancy matrix. The
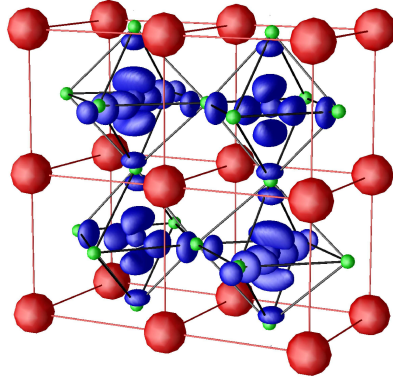
Fig. 9. The $I4/mcm$ primitive cell and hole orbital order as obtained by the GGA+DMFT calculation for paramagnetic KCuF$_3$ with $\delta_{\mathrm{JT}} = 4.4\%$ is shown. The fluorine atoms and fluorine octahedra are shown in green, the potassium in red, and the Wannier Cu e_g charge density in blue. The local coordinate system is chosen with the z direction defined along the longest Cu-F bond of the CuF$_6$ octahedron.

double-counting correction $E_{\mathrm{DC}} = \frac{1}{2}UN_{e_g}(N_{e_g} - 1) - \frac{1}{4}JN_{e_g}(N_{e_g} - 2)$ corresponds to the average Coulomb repulsion between the N_{e_g} electrons in the Cu e_g Wannier orbitals. Since the Hamiltonian involves only correlated orbitals the number of Wannier electrons N_d is conserved. Therefore, the double-counting correction amounts to an irrelevant shift of the total energy.

In Fig. 8 (left panel) we present our results for the GGA+DMFT total energy as a function of the JT distortion δ_{JT}. The inclusion of the electronic correlations among the partially filled Cu e_g states in the GGA+DMFT approach is seen to lead to a very substantial lowering of the total energy by ~ 175 meV per formula unit. This implies that the strong JT distortion persists up to the melting temperature (> 1000 K), in agreement with experiment. The minimum of the GGA+DMFT total energy is located at the value $\delta_{\mathrm{JT}} = 4.2\%$, which is also in excellent agreement with the experimental value of 4.4% [111]. This clearly shows that the JT distortion in paramagnetic KCuF$_3$ is caused by electronic correlations.

In Fig. 8 (right panel) we show the spectral density of paramagnetic KCuF$_3$ calculated for several δ_{JT} values using the maximum entropy method. The GGA+DMFT calculations give a paramagnetic insulating state with a substantial orbital polarization for all δ_{JT} considered here. The energy gap is in the range 1.5-3.5 eV, and increases with increasing of δ_{JT}. The sharp feature in the spectral density at about -3 eV corresponds to the fully occupied $3z^2 - r^2$ orbital [125], whereas the lower and upper Hubbard bands are predominantly of $x^2 - y^2$ character and are located at -5.5 eV and 1.8 eV, respectively. The corresponding Cu e_g Wannier charge density calculated for the experimental value of JT distortion of 4.4% is presented in Fig. 9. The GGA+DMFT results clearly show an alternating occupation of the Cu $d_{x^2-z^2}$ and $d_{y^2-z^2}$ hole orbitals which implies antiferro-orbital order. Moreover, we have proved the stability of the paramagnetic solution at high temperatures (560 K) with respect to the A-type antiferromagnetic one. In this calculation we have used the experimental room-temperature crystal structure of KCuF$_3$ with $\delta_{\mathrm{JT}} = 4.4\%$ and long-range A-type antiferromagnetic order. However, in agreement with experiment, the calculation gives paramagnetic insulating solution with the orbital order as it has been found above.

We now perform a structural optimization of paramagnetic KCuF$_3$. For simplicity, we consider only two independent structural parameters, the lattice constant a and the JT distortion δ_{JT}. In this calculation we keep unchanged the space group symmetry (tetragonal $I4/mcm$) and the experimental value of the unit cell volume (taken at the ambient pressure at room temperature) [111]. We first calculate the non-magnetic GGA electronic structure for different values of δ_{JT} and lattice constant a. In Fig. 10 (left panel) we display the GGA total energies for different JT distortion δ_{JT} as a function of the lattice constant a. The data points were further interpolated by smooth curves. The result of the total energy variation, namely, the line connecting the minima of the corresponding curves, is shown in bold (blue) line. We find that
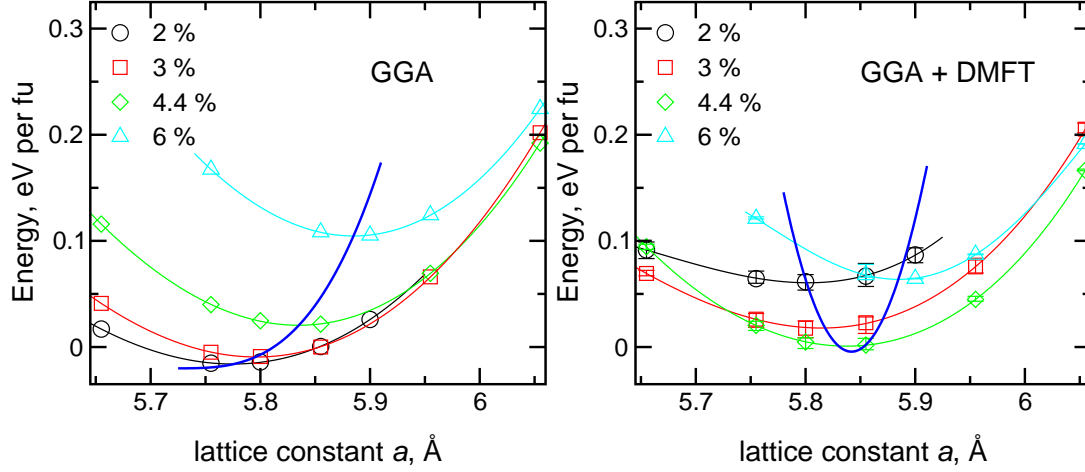
Fig. 10. Comparison of the total energies of paramagnetic $KCuF_3$ computed by GGA (left panel) and GGA+DMFT(QMC) (right panel) for different values of the JT distortion δ_{JT} as a function of the lattice constant a [104]. The result of the total energy variation is shown as the thick blue line. Error bars indicate the statistical error of the DMFT(QMC) calculations.

the variation of the GGA total energy, is seen to be constant for $\delta_{JT} < 2\%$ with the end point at $a \sim 5.75$ Å. This implies the absence of the cooperative JT distortion and results in a nearly cubic ($c/a \approx 1.0$) unit cell, which is in clear contradiction to experiment [111].

To proceed further, we construct the effective low-energy Hamiltonian for the partially filled Cu e_g orbitals for each value of the JT distortion δ_{JT} and the lattice constant a considered here, and compute the corresponding GGA+DMFT total energy (see Fig. 10, right panel) [103,104]. In contrast to the GGA result, the inclusion of the electronic correlations among the partially filled Cu e_g states in the GGA+DMFT method not only correctly describes the spectral properties, but also leads to a very prominent minimum in the resulting total energy variation. The minimum is located at the value $a = 5.842$ Å and $\delta_{JT} \approx 4.13\%$, which is in excellent agreement with experimental value $a = 5.855$ Å and $\delta_{JT} \approx 4.4\%$. In addition, the structural optimization within GGA+DMFT predicts the correct tetragonal compression of the unit cell $c/a \approx 0.95$ [111].

4.2 Application to LaMnO$_3$

LaMnO$_3$ is another prototypical material with respect to the cooperative Jahn-Teller effect and orbital order. At room-temperature it is an orthorhombic perovskite with a GdFeO$_3$-like crystal structure and space group $Pnma$ [128]. The Mn ions have octahedral oxygen surrounding and are in a high-spin $3d^4$ electronic configuration due to Hund's rule coupling, with three electrons in the $t_{2g\uparrow}$ orbitals and a single electron in an $e_{g\uparrow}$ orbital ($t_{2g}^3 e_g^1$ orbital configuration). The two types of structural instabilities give rise to the changes relative to the cubic perovskite structure. The first is related to a large ion-size misfit parameter $\sqrt{2}(R_O + R_{Mn})/(R_O + R_{La})$ which favors rotations of the octahedra to accommodate a more efficient unit cell space filling; R_{Mn}, R_{La}, and R_O are the ionic radii of Mn, La, and O ions, respectively. The second is a JT instability due to the e_g-orbital degeneracy which is lifted due to a cooperative JT distortion, leading to an alternating occupation of $d_{3x^2-r^2}$ and $d_{3y^2-r^2}$ electron orbitals in the ab plane (antiferro-orbital ordering) and to a tetragonal compression of the unit cell. The rotations of the octahedra lower the symmetry further, finally resulting in the orthorhombic unit cell. The JT distortion experimentally persists up to $T_{JT} \approx 750$ K which is remarkably higher than the Néel temperature of ~ 140 K. Above T_{JT} LaMnO$_3$ undergoes a structural phase transition [129], with volume collapse [130] to a nearly cubic structure in which orbital order and JT distortion vanish [129]. Below $T_N \sim 140$ K LaMnO$_3$ shows A-type long-range antiferromagnetic order

consistent with the Goodenough-Kanamori-Anderson rules for a superexchange interaction with $d_{3x^2-r^2}/d_{3y^2-r^2}$ antiferro-orbital order [128,129].

The LDA+U approach is found to give, at equilibrium, the correct insulating behavior of the low-temperature antiferromagnetic phase and a JT distortion in satisfactory agreement with experiment [131]. Nevertheless, it should be noted again that the application of this approach is limited to temperatures below T_N. Therefore, LDA+U cannot describe the properties of LaMnO$_3$ at $T > T_N$ and, in particular, at room temperature, where LaMnO$_3$ is a correlated *paramagnetic* insulator with a robust JT distortion. Nonmagnetic LDA/GGA calculations instead give a *metal* and cannot explain the insulating paramagnetic behavior at $T > T_N$. The electronic properties of paramagnetic LaMnO$_3$ have already been studied using the LDA+DMFT approach [132,133,134,135]. However, no attempt has been made to determine the structural properties and, in particular, the value of the cooperative JT distortion so far. Here we investigate the stability of the cooperative JT distortion and perform a structural optimization of paramagnetic LaMnO$_3$. To determine the electronic and structural properties we employ the novel GGA+DMFT scheme implemented with plane-wave pseudopotentials [103,104,105].

We first compute the nonmagnetic GGA band structure of paramagnetic LaMnO$_3$ using the plane-wave pseudopotential approach as in the case of KCuF$_3$. In this calculation, we have used the orthorhombic *Pnma* crystal structure as reported by Elemans *et al.*, with lattice constants $a = 5.742$, $b = 7.668$, and $c = 5.532$ Å [128]. The calculation was performed for different values of JT distortion δ_{JT}, which is now defined as the ratio between the difference of the long (d_l) and the short (d_s) bond distances and the mean Mn-O distance in the basal *ab* plane, i.e., $\delta_{\mathrm{JT}} = 2(d_l - d_s)/(d_l + d_s)$. Structural data [128] yield $\delta_{\mathrm{JT}} = 0.138$. Here we change only the parameter δ_{JT} ($0 \leq \delta_{\mathrm{JT}} \leq 0.2$) while the value of the MnO$_6$ octahedron tilting and rotation was fixed.

For all values of δ_{JT} considered here we find a metallic solution with a considerable orbital polarization due to the crystal field splitting. Overall, these results qualitatively agree with previous band structure calculations [136], namely, GGA cannot describe a paramagnetic insulating behavior which is found in experiment. We notice that even for the large δ_{JT} value of 0.2 ($\sim 45\%$ larger than found in experiment [128]) the GGA calculations predict a metal. In Fig. 11 (left panel) we display our results for the GGA total energy as a function of the JT distortion δ_{JT}. The GGA total energy is almost parabolic which implies the absence of a cooperative JT distortion. Altogether, the non-magnetic GGA calculations give a metallic solution without cooperative JT distortion that contradicts experiment [128,129]. This implies the importance of electronic correlations to describe the experimentally observed insulating behavior and orbital order in paramagnetic LaMnO$_3$.

To proceed further, we turn to the GGA+DMFT results where we treat the Mn e_g orbitals as correlated orbitals. To achieve this we employ the GGA results and make a projection onto atomic-centered symmetry-constrained Mn e_g Wannier orbitals [51,52,105]. In this calculation we assume that three (among the $3d^4$ electronic configuration) electrons are localized in the t_{2g} orbitals. Therefore, they are treated as classical spins S, with a random orientation above T_N (i.e., there is no correlation between different Mn sites), which couple to the e_g electron with an energy JS. This coupling can be estimated as the energy of the splitting of the $e_{g\uparrow}$ and $e_{g\downarrow}$ bands in the ferromagnetic band-structure calculations and gives an additional term in the Hamiltonian (5), namely,

$$\hat{H} = \hat{H}_{\mathrm{GGA}} + U \sum_{im} \hat{n}_{im\uparrow} \hat{n}_{im\downarrow} - JS \sum_{im} (\hat{n}_{im\uparrow} - \hat{n}_{im\downarrow}) + \sum_{i\sigma\sigma'} (V - \delta_{\sigma\sigma'} J) \hat{n}_{i1\sigma} \hat{n}_{i2\sigma'} - \hat{H}_{\mathrm{DC}}. \quad (8)$$

This corresponds to the ferromagnetic Kondo-lattice model Hamiltonian with an on-site Coulomb repulsion between e_g electrons, which has been intensively studied as a possible microscopic model to explain the colossal magnetoresistance in manganites [138,139]. We note that in order to calculate the total energy one needs to modify Eq. 6 by adding the expectation value of the JS term which describes the total energy gain due to the spin polarization of the e_g orbitals at the Mn site. We take the local Coulomb repulsion $U = 5$ eV, the Hund's rule exchange $J = 0.75$ eV, and $2JS = 2.7$ eV from the literature [133,134], and further solve the many-body Hamiltonian (8) for each value of δ_{JT} using the single-site DMFT with Hirsch-Fye
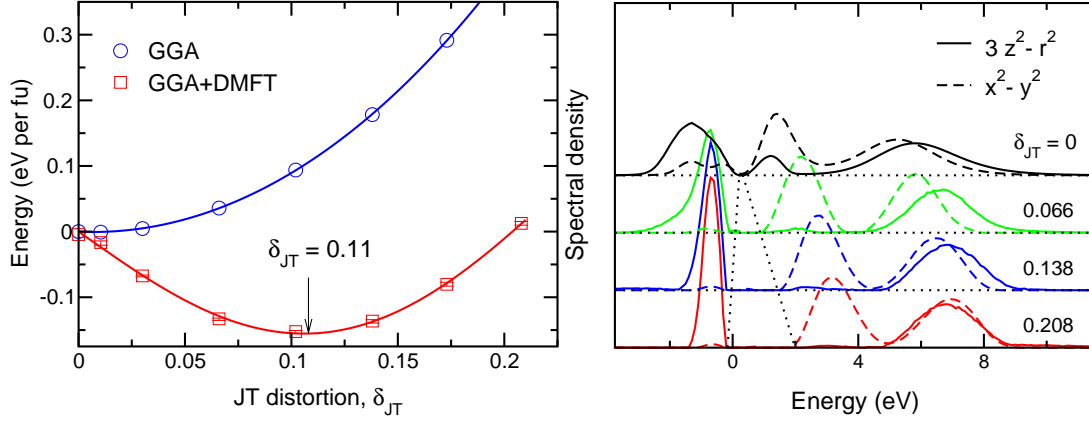
Fig. 11. Left panel: Comparison of the total energies of paramagnetic LaMnO$_3$ computed by GGA and GGA+DMFT (QMC) as a function of the JT distortion [104]. Error bars indicate the statistical error of the DMFT(QMC) calculations. Right panel: Orbitally resolved Mn e_g spectral densities of paramagnetic LaMnO$_3$ as obtained by GGA+DMFT(QMC) for different values of the JT distortion. The resulting orbitally resolved spectral density shown by solid [dashed] line is predominantly of $3z^2-r^2$ [x^2-y^2] character (in the local frame [137]).

quantum Monte Carlo (QMC) calculations [53,126]. Again the calculations were performed at $T = 1160$ K ($\beta = 10$ eV^{-1}), using 40 imaginary-time slices [127].

In Fig. 11 (left panel) we display the GGA+DMFT total energy calculated as a function of the JT distortion δ_{JT}. In contrast to the GGA result, GGA+DMFT yields a substantial total energy gain of ~ 150 meV per formula unit. This implies that the cooperative JT distortion indeed persists up to high temperatures ($T > 1000$ K), while in GGA a JT distortion does not occur at all. Taking into account that the calculations have been performed for the low-temperature crystal structure of LaMnO$_3$ [128] this estimate (150 meV) is in good agreement with $T_{JT} \sim 750$ K at which the JT distortion vanishes [129,130]. The minimum of the GGA+DMFT total energy is located at the value $\delta_{JT} \sim 0.11$, which is also in good agreement with the experimental value of 0.138 [128,129]. We note that GGA+DMFT calculations correctly describe both electronic and structural properties of paramagnetic LaMnO$_3$. This shows that the JT distortion in paramagnetic LaMnO$_3$ is caused by electronic correlations.

In Fig. 11 (right panel) we display the spectral density of paramagnetic LaMnO$_3$ calculated for several δ_{JT} values using the maximum entropy method. We find a strong orbital polarization for large δ_{JT}, which gradually decreases for decreasing JT distortion. The occupied part of the e_g density is located at about -2 to -1 eV and corresponds to the e_g states with spin parallel to the t_{2g} spin at that site. It has predominantly Mn $d_{3x^2-r^2}$ and $d_{3y^2-r^2}$ orbital character with a considerable admixture of $d_{z^2-r^2}$ for small JT distortions. The energy gap is about 2 eV for large δ_{JT} and considerably decreases with decreasing δ_{JT}, resulting in a pseudogap behavior at the Fermi level for $\delta_{JT} = 0$. In Fig. 12 we present the corresponding Mn e_g Wannier charge density computed for the experimental JT distortion value of $\delta_{JT} = 0.138$. The result clearly indicates an alternating occupation of the Mn $d_{3x^2-r^2}$ and $d_{3y^2-r^2}$ orbitals, corresponding to the occupation of a $3z^2 - r^2$ orbital in the local frame [137], which implies antiferro-orbital order. Thus, in agreement with experiment, the calculations give a paramagnetic insulating solution with antiferro-orbital order and stable JT distortion.

To conclude, we presented applications of the novel GGA+DMFT approach to two prototypical Jahn-Teller materials, KCuF$_3$ and LaMnO$_3$, and computed the orbital order and cooperative JT distortion in these compounds. In particular, our results obtained for the paramagnetic phase of KCuF$_3$ and LaMnO$_3$, namely an equilibrium Jahn-Teller distortion δ_{JT} of 4.2% and 0.11, respectively, and antiferro-orbital order, agree well with experiment. The present approach overcomes the limitations of the LDA+U method and previous implementations of LDA+DMFT and is able to determine correlation-induced structural transformations in both
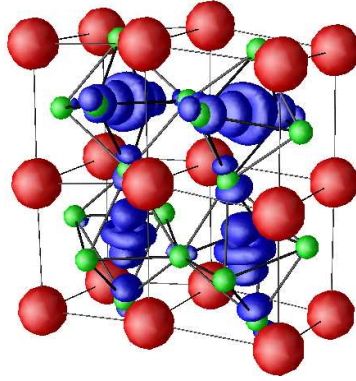
Fig. 12. The *Pnma* primitive cell and orbital order as obtained by the GGA+DMFT calculation for paramagnetic LaMnO$_3$ with $\delta_{\mathrm{JT}} = 0.138$ is shown. The oxygen atoms and oxygen octahedra are shown in green, the lanthanum in red, and the Wannier Mn e_g charge density in blue.

paramagnetic and long-range magnetically ordered solids. Thereby it can be employed for the lattice optimization and molecular-dynamic simulations of these systems. The computational scheme presented here allows us to investigate complex materials with strong electronic interactions and correlation-induced structural transformations, shifts of equilibrium atomic positions and changes in the lattice structure, and to perform a structural optimization of *paramagnetic* solids. It opens the way for fully microscopic investigations of the structural properties of strongly correlated electron materials such as lattice instabilities observed at correlation-induced metal-insulator transitions.

5 Kinks in the dispersion of correlated materials

The electronic dispersion relation indicates at which energy and crystal momentum one-particle excitations can occur in a solid. Interactions between electrons influence not only the shape and position of the dispersion, but also make the lifetime of such excitations finite. A robust general definition for the branches of the dispersion relation $E_{\boldsymbol{k}}$ is provided by the local maxima of the spectral function $A(\boldsymbol{k}, \omega)$, i.e., its peak locations as a function of ω for a given momentum $\boldsymbol{k}$. For energies ω far from the Fermi surface, the peaks in the spectral function of a strongly interacting material can be quite broad, corresponding to incoherent excitations with a short lifetime. Nevertheless the maxima in $A(\boldsymbol{k}, \omega)$ are always well defined, even if their location might be difficult to determine from angle-resolved photoemission data at high binding energies. The excitations for energies close to the Fermi surface, on the other hand, are coherent in a Landau-Fermi liquid, i.e., they are only weakly damped and correspond to sharp peaks in the spectral function. In this case the correlated dispersion is given by the uncorrelated dispersion multiplied by a renormalization factor Z related to Fermi-liquid parameters.

A characteristic feature of strongly correlated metals is a transfer of spectral weight into the lower and upper Hubbard bands due to the Coulomb interaction. Together with the central peak near the Fermi energy the momentum-integrated spectral function therefore typically has three peaks. One exemplary material with this type of spectrum is the cubic perovskite SrVO$_3$ with $3d^1$ electronic configuration, leading to band-filling of one electron per site in the threefold-degenerate t_{2g} bands. To obtain its momentum-resolved spectral function with LDA+DMFT, we used Nth order muffin orbitals (NMTO) to obtain the downfolded 3×3 Hamiltonian for the t_{2g} bands [140]. For the DMFT calculation the Coulomb interaction parameters for these bands are $U = 5.55$ eV for the on-site repulsion, $J = 1.0$ eV for the Hund's exchange coupling, and $U' = 3.55$ eV for the interorbital Coulomb repulsion [141]. The local (momentum-integrated) spectral function has an asymmetric three-peak structure with a high central peak and two smaller peaks due to the Hubbard bands [140]. The total spectral function $A(\boldsymbol{k}, \omega)$ is shown in the intensity plot in Fig. 13, with its local maxima marked by white dots. Remarkably, the dispersion $E_{\boldsymbol{k}}$
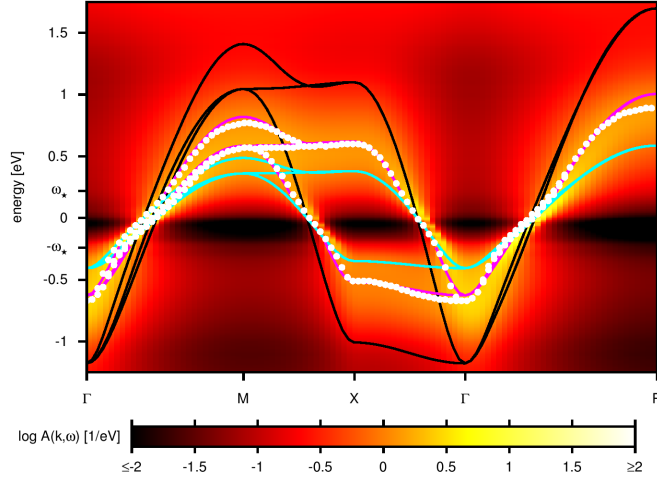
Fig. 13. Intensity plot of the total spectral function for $SrVO_3$ obtained with LDA+DMFT; after [140]. Near the Fermi energy the dispersion $E_{\boldsymbol{k}}$ (white dots) is given by the renormalized LDA band structure $\epsilon_{\boldsymbol{k}}$ (black lines) with a Fermi-liquid factor $Z = 0.35$, i.e. $E_{\boldsymbol{k}} = Z\epsilon_{\boldsymbol{k}}$ (blue line). For higher energies the dispersion relation follows the LDA band structure with a different renormalization, $E_{\boldsymbol{k}} = Z'\epsilon_{\boldsymbol{k}} + c_{\pm}$ (pink line), with $Z' = 0.64$, $c_+ = 0.086$ eV, $c_- = 0.13$ eV [142]. The crossover between the two slopes leads to kinks at energies $\omega_{\star,+} = 0.22$ eV and $\omega_{\star,-} =$ -0.24 eV in the effective dispersion. The parameter values given here are calculated from the theory of Ref. [142]; due to the shift $c_{\pm}$ the parameter Z' differs from the fitted parameter in Ref. [140] without shift.

shows a small sudden change in slope near energies $\omega_{\star} \approx 0.25$ eV. There a crossover between two regimes occurs: In the low-energy Fermi-liquid regime, $|\omega| < \omega_{\star}$, the LDA dispersion $\epsilon_{\boldsymbol{k}}$ is renormalized by the Landau parameter Z so that $E_{\boldsymbol{k}} = Z\epsilon_{\boldsymbol{k}}$. On the other hand, at higher energies, outside the Fermi-liquid regime but still inside the central peak, the dispersion is given by $E_{\boldsymbol{k}} = Z'\epsilon_{\boldsymbol{k}}$ with a different renormalization factor. In Ref. [140] these parameters were determined as $Z = 0.33$ and $Z' = 0.53$, i.e., the renormalization is much stronger near the Fermi surface. This value of $Z' \approx 0.5$ was also found in ARPES experiments [143,144]. Although no sharp kink was found, a weak change in slope was detected at $\omega \approx -0.2$ eV [144], in agreement with the LDA+DMFT calculation.

These kinks in the dispersion can be understood from a microscopic theory [142], which correctly predicts the renormalized bandstructure outside the Fermi-liquid regime only from Fermi-liquid parameters and the uncorrelated spectrum. A sufficiently strong interaction is needed, so that the local spectral function has a three-peak structure with a central peak and two Hubbard peaks. In the absence of particle-hole symmetry this condition can be relaxed; e.g., it suffices that the central peak is well separated from the lower Hubbard peak for a kink to develop below the Fermi surface. As we will now discuss, the dips on the sides of the central peak lead to kinks in the dispersion inside the central peak; for simplicity, we consider only a one-band system with symmetric spectrum (Fig. 14). Namely, well-separated peaks in the local spectral function $A(\omega) = -\text{Im}[G(\omega)/\pi]$ (top panel in Fig. 14) have the consequence that due to Kramers-Kronig relations, $\text{Re}[G(\omega)]$ must have sharp maxima at energies ω_{max} inside the central spectral peak (second panel from top in Fig. 14). These maxima induce kinks in the self-energy $\Sigma(\boldsymbol{k}, \omega)$, which lead to kinks in the $\boldsymbol{k}$-resolved spectral function, $A(\boldsymbol{k}, \omega) = -\text{Im}[\omega + \mu - \epsilon_{\boldsymbol{k}} - \Sigma(\boldsymbol{k}, \omega)]^{-1}/\pi$, and thus in the dispersion. In DMFT the self-energy is independent of momentum, $\Sigma(\boldsymbol{k}, \omega) = \Sigma(\omega)$, and related to the local Green function by the self-consistency condition, $\Sigma(\omega) = \omega + \mu - 1/G(\omega) - \Delta(G(\omega))$, where $\Delta(G(\omega))$ is the hybridization function. For a three-peak spectral function $A(\omega)$, the term $\text{Re}[\omega + \mu - 1/G(\omega)]$ is essentially linear inside the central peak (bottom panel in Fig. 14). By contrast, $\Delta(G(\omega))$, which can be expanded in powers of $G(\omega)$, always contains a term linear in $G(\omega)$. As a consequence $\Sigma(\omega)$ always has a contribution from the peaks in $\text{Re}[G(\omega)]$ that is nonlinear in ω inside the central
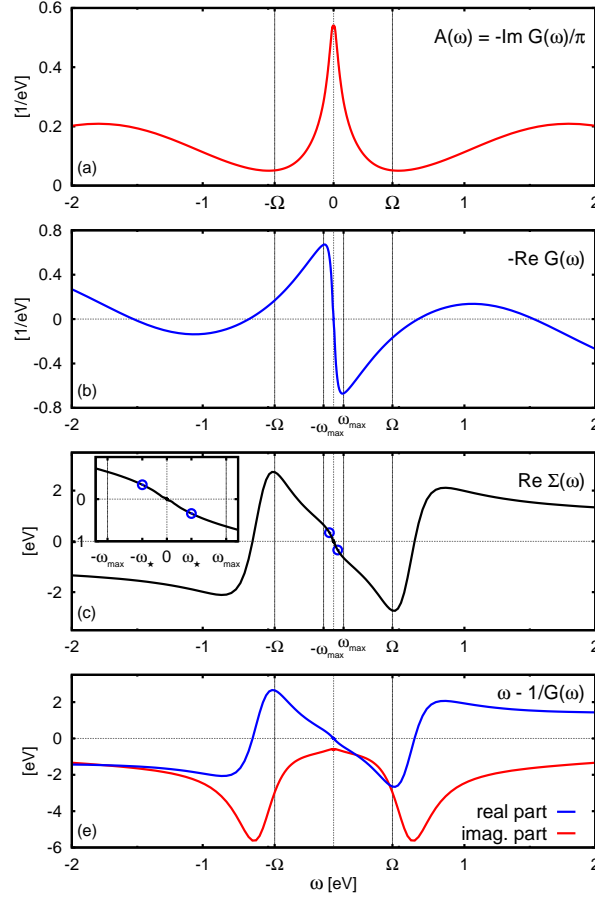
Fig. 14. Origin of kinks in a strongly correlated system (one-band Hubbard model in DMFT with $Z = 0.086$) [142]. From top to bottom: Local spectral function with three well-separated peaks; corresponding real part of the local Green function with peaks inside central spectral peak; real part of the self-energy, in which the maxima of $\mathrm{Re}[G(\omega)]$ translate into kinks; $\omega - 1/G(\omega)$, which contributes only a smooth linear background to $\mathrm{Re}[\Sigma(\omega)]$.

peak. Thus $\mathrm{Re}[\Sigma(\omega)]$ has two different slopes for $|\omega|$ smaller or larger than $\omega_\star$. This translates into the usual Fermi-liquid renormalization $E_{\boldsymbol{k}} = Z\epsilon_{\boldsymbol{k}}$ near the Fermi energy, but a shifted and renormalized dispersion $E_{\boldsymbol{k}} = Z'\epsilon_{\boldsymbol{k}} + \text{const}$ for higher binding energies [142]. From the Fermi-liquid renormalization Z and the non-interacting bandstructure the constant shift, the parameter Z' and the crossover energy $\omega_\star$ can be obtained explicitly [142]; in particular Z' and $\omega_\star$ are proportional to the Fermi-liquid parameter Z (multiplied by an uncorrelated scale). The values for $SrVO_3$ are listed in Fig. 13 and fit the correlated dispersion very well.

According to the theory described above the kinks in the slope of the dispersion are a direct consequence of the electronic interaction [142]. They can lead to corresponding kinks in the low-temperature electronic specific heat [145]. The presence of kinks has also been linked to maxima in the spin susceptibility [146]. Of course, additional kinks in the electronic dispersion may arise from the coupling of electrons to bosonic degrees of freedom, such as phonons. Recent experiments have found evidence for kinks in Ni(110) [147], which may be due to the electronic mechanism presented here.

6 Summary

The combination of dynamical mean-field theory (DMFT) with LDA/GGA electronic structure calculations has led to important advances in our understanding and in the quantitative description of correlated electron materials. For example, by including the p-d hybridization into the LDA+DMFT scheme it is now possible to clearly distinguish between Mott-Hubbard and charge-transfer insulators. This allowed for the computation of the local correlations and hole doping in NiO. By treating the local correlations and the Ni $3d$ - O2 p hybridization on the same footing we were able to provide a description of the full valence-band and conduction-band spectra of charge-transfer systems with strong hybridization. These results provide a quantitative explanation of the experimental photoemission, inverse photoemission, and ARPES data. Our results show that, provided the p-d hybridization is explicitly included, the LDA+DMFT is able to treat the late transition-metal oxides and charge-transfer systems in general.

In a second application we investigated the metallization and magnetic-moment collapse in MnO and Fe_2O_3. Our results not only describe the experimentally observed simultaneous collapse of the magnetic moment and the volume in MnO but also explain the origin of the collapse of the magnetic moment which originates from the increase of the crystal field splitting and not from the change of the band width. Since similar results were obtained for hematite (Fe_2O_3) we may conclude that the transition in this compound at about 50 GPa may be described by an electronically driven volume collapse.

Our formulation of GGA+DMFT in terms of plane-wave pseudopotentials provides a robust computational scheme for the investigation of complex correlated materials. We applied this novel approach to explain various electronic and structural properties of the two prototypical Jahn-Teller materials $KCuF_3$ and $LaMnO_3$ in their correlated paramagnetic phase. Our results for the equilibrium cooperative JT distortion, the lattice constants, and the antiferro-orbital order agree well with experiment. This computational scheme will make it possible to investigate correlation induced structural transformations, shifts of equilibrium atomic positions, and changes in the lattice structure, and to perform the structural optimization of correlated *paramagnetic* solids. This opens the way for fully microscopic investigations of lattice instabilities which are known to occur in the vicinity of correlation-induced metal-insulator transitions.

Finally, we offered a comprehensive explanation of kinks in the effective dispersion of correlated electrons in correlated materials with a pronounced three-peak structure. In particular we found that Landau quasiparticles exist only in a remarkably narrow region around the Fermi energy. For higher energies, but still in the central maximum of the spectral function, the excitations are described by a different dispersion relation which may be calculated analytically. The transition from one to the other regime is relatively sharp and leads to the kinks in the dispersion relation. One of the most astonishing results of this investigation is the fact that it is possible to describe properties of the system outside the Landau-Fermi-liquid regime fully analytically.

In view of the rapid developments of the LDA+DMFT scheme during the last couple of years it is clear that this approach has a great potential for further developments. It is already foreseeable that the LDA+DMFT approach will even be able to explain and predict the properties of complex correlated electron materials.

References

1. M. Imada, A. Fujimori, Y. Tokura, Rev. Mod. Phys. **70**, 1039 (1998)
2. Y. Tokura, N. Nagaosa, Science **288**, 462 (2000)
3. E. Dagotto, Science **309**, 257 (2005)
4. R. O. Jones, O. Gunnarsson, Rev. Mod. Phys. **61**, 689 (1989)
5. J. P. Perdew, K. Burke, M. Ernzerhof, Phys. Rev. Lett. **77**, 3865 (1996)

6. F. Tran, P. Blaha, Phys. Rev. Lett. **102**, 226401 (2009)

7. V. I. Anisimov, J. Zaanen, O. K. Andersen, Phys. Rev. B **44**, 943 (1991)

8. A. I. Liechtenstein, V. I. Anisimov, J. Zaanen, Phys. Rev. B **52**, R5467 (1995)

9. V. I. Anisimov, F. Aryasetiawan, A. I. Lichtenstein, J. Phys.: Condens. Matter **9**, 767 (1997)

10. S. Baroni, S. de Gironcoli, A. Dal Corso, P. Giannozzi, Rev. Mod. Phys. **73**, 515 (2001)

11. P. Giannozzi, S. Baroni, N. Bonini, M. Calandra, R. Car, C. Cavazzoni, D. Ceresoli, G. L. Chiarotti, M. Cococcioni, I. Dabo, A. Dal Corso, S. Fabris, G. Fratesi, S. de Gironcoli, R. Gebauer, U. Gerstmann, C. Gougoussis, A. Kokalj, M. Lazzeri, L. Martin-Samos, N. Marzari, F. Mauri, R. Mazzarello, S. Paolini, A. Pasquarello, L. Paulatto, C. Sbraccia, S. Scandolo, G. Sclauzero, A. P. Seitsonen, A. Smogunov, P. Umari, R. M. Wentzcovitch, J. Phys. Condens. Matter **21**, 395502 (2009)

12. P. Blaha, K. Schwarz, G. Madsen, D. Kvasnicka, J. Luitz, WIEN2k, *An Augmented Plane Wave + Local Orbitals Program for Calculating Crystal Properties* (Karlheinz Schwarz, Techn. Universität Wien, Austria), 2001.

13. G. Kresse, J. Hafner, Phys. Rev. B **47**, 558 (1993)

14. W. Metzner, D. Vollhardt, Phys. Rev. Lett. **62**, 324 (1989)

15. A. Georges, G. Kotliar, W. Krauth, M. J. Rozenberg, Rev. Mod. Phys. **68**, 13 (1996)

16. G. Kotliar, D. Vollhardt, Phys. Today **57**, 53 (2004)

17. G. Kotliar, S. Y. Savrasov, K. Haule, V. S. Oudovenko, O. Parcollet, C. A. Marianetti, Rev. Mod. Phys. **78**, 865 (2006)

18. M. I. Katsnelson, V. Yu. Irkhin, L. Chioncel, A. I. Lichtenstein, R. A. de Groot, Rev. Mod. Phys. 80, 315 (2008)

19. V. I. Anisimov, A. I. Poteryaev, M. A. Korotin, A. O. Anokhin, G. Kotliar, J. Phys. Condens. Matt. **9**, 7359 (1997)

20. A. I. Lichtenstein, M. I. Katsnelson, Phys. Rev. B **57**, 6884 (1998)

21. A. I. Lichtenstein, M. I. Katsnelson, G. Kotliar, in *Electron Correlations and Materials Properties 2nd ed.*, edited by A. Gonis, N. Kioussis, M. Ciftan (Kluwer Academic/Plenum, New York, 2002), p. 428

22. K. Held, I. A. Nekrasov, G. Keller, V. Eyert, N. Blümer, A. K. McMahan, R. T. Scalettar, Th. Pruschke, V. I. Anisimov, D. Vollhardt, Psi-k Newsletter **56**, 65 (2003);

23. K. Held, I. A. Nekrasov, G. Keller, V. Eyert, N. Blümer, A. K. McMahan, R. T. Scalettar, Th. Pruschke, V. I. Anisimov, D. Vollhardt, Phys. Status Solidi B **243**, 2599 (2006)

24. K. Held, Adv. Phys. 56, 829 (2007)

25. K. Held, G. Keller, V. Eyert, D. Vollhardt, V. I. Anisimov, Phys. Rev. Lett. **86**, 5345 (2001)

26. E. Pavarini, S. Biermann, A. Poteryaev, A. I. Lichtenstein, A. Georges, O. K. Andersen, Phys. Rev. Lett. **92**, 176403 (2004)

27. A. I. Poteryaev, A. I. Lichtenstein, G. Kotliar, Phys. Rev. Lett. **93**, 086401 (2004)

28. S. Biermann, A. Poteryaev, A. I. Lichtenstein, A. Georges, Phys. Rev. Lett. **94**, 026404 (2005)

29. L. Chioncel, Ph. Mavropoulos, M. Lezaić, S. Blügel, E. Arrigoni, M. I. Katsnelson, A. I. Lichtenstein, Phys. Rev. Lett. **96**, 197203 (2006)

30. K. Held, A. K. McMahan, R. T. Scalettar, Phys. Rev. Lett. **87**, 276404 (2001)

31. A. K. McMahan, K. Held, R. T. Scalettar, Phys. Rev. B **67**, 075108 (2003)

32. B. Amadon, S. Biermann, A. Georges, F. Aryasetiawan, Phys. Rev. Lett. **96**, 066402 (2006); see also L. V. Pourovskii, B. Amadon, S. Biermann, A. Georges, Phys. Rev. B **76**, 235101 (2007) where the authors discuss the problem of full self-consistency over the charge density in γ-Ce and Ce_2O_3.

33. S. Y. Savrasov, G. Kotliar, E. Abrahams, Nature (London) **410**, 793 (2001)

34. X. Dai, S. Y. Savrasov, G. Kotliar, A. Migliori, H. Ledbetter, E. Abrahams, Science **300**, 953 (2003)

35. S. Y. Savrasov, G. Kotliar, Phys. Rev. B **69**, 245101 (2004)

36. M. I. Katsnelson, A. I. Lichtenstein Phys. Rev. B **61**, 8906 (2000)

37. A. I. Lichtenstein, M. I. Katsnelson, G. Kotliar, Phys. Rev. Lett. **87**, 067205 (2001)

38. J. Braun, J. Minár, H. Ebert, M. I. Katsnelson, A. I. Lichtenstein, Phys. Rev. Lett. **97**, 227601 (2006)

39. A. Grechnev, I. Di Marco, M. I. Katsnelson, A. I. Lichtenstein, J. Wills, O. Eriksson, Phys. Rev. B **76**, 035107 (2007)

40. S. Chadov, J. Minár, M. I. Katsnelson, H. Ebert, D. Ködderitzsch, A. I. Lichtenstein, Europhys. Lett. **82**, 37001 (2008)

41. J. Kuneš, V. I. Anisimov, A. V. Lukoyanov, D. Vollhardt, Phys. Rev. B **75**, 165115 (2007)

42. J. Kuneš, V. I. Anisimov, S. L. Skornyakov, A. V. Lukoyanov, D. Vollhardt, Phys. Rev. Lett. **99**, 156404 (2007)

43. J. Kuneš, A. V. Lukoyanov, V. I. Anisimov, R. T. Scalettar, W. E. Pickett, Nature Materials **7**, 198 (2008)

44. J. Kuneš, Dm. M. Korotin, M. A. Korotin, V. I. Anisimov, P. Werner, Phys. Rev. Lett. **102**, 146402 (2009)

45. J. Zaanen, G. A. Sawatzky, J. W. Allen, Phys. Rev. Lett. **55**, 418 (1985)

46. G. A. Sawatzky, J. W. Allen, Phys. Rev. Lett. **53**, 2339 (1984)

47. D. E. Eastman, J. L. Freeouf, Phys. Rev. Lett. **34**, 395 (1975)

48. Z.-X. Shen, C. K. Shih, O. Jepsen, W. E. Spicer, I. Lindau, J. W. Allen, Phys. Rev. Lett. **64**, 2442 (1990)

49. Z.-X. Shen, R. S. List, D. S. Dessau, B. O. Wells, O. Jepsen, A. J. Arko, R. Barttlet, C. K. Shih, F. Parmigiani, J. C. Huang, P. A. P. Lindberg, Phys. Rev. B **44**, 3604 (1991)

50. O. Tjernberg, S. Söderholm, G. Chiaia, R. Girard, U. O. Karlsson, H. Nylén, I. Lindau, Phys. Rev. B **54**, 10245 (1996)

51. N. Marzari, D. Vanderbilt, Phys. Rev. B **56**, 12847 (1997)

52. V. I. Anisimov, D. E. Kondakov, A. V. Kozhevnikov, I. A. Nekrasov, Z. V. Pchelkina, J. W. Allen, S.-K. Mo, H.-D. Kim, P. Metcalf, S. Suga, A. Sekiyama, G. Keller, I. Leonov, X. Ren, D. Vollhardt, Phys. Rev. B **71**, 125119 (2005)

53. J. E. Hirsch, R. M. Fye, Phys. Rev. Lett **56**, 2521 (1986)

54. M. Jarrell, J. E. Gubernatis, Phys. Rep. **269**, 133 (1996)

55. A. Fujimori, F. Minami, S. Sugano, Phys. Rev. B **29**, 5225 (1984)

56. J. van Elp, H. Eskes, P. Kuiper, G. A. Sawatzky, Phys. Rev. B **45**, 1612 (1992)

57. S. V. Faleev, M. van Schilfgaarde, T. Kotani, Phys. Rev. Lett. **93**, 126406 (2004)

58. J.-L. Li, G.-M. Rignanese, S. G. Louie, Phys. Rev. B **71**, 193102 (2005)

59. S. Sharma, S. Shallcross, J. K. Dewhurst, E. K. U. Gross, arXiv:0912.1118

60. S. Kobayashi, Y. Nohara, S. Yamamoto, T. Kujiwara, Phys. Rev. B **70**, 155112 (2008)

61. C. Rödl, F. Fuchs, J. Furthmüller, F. Bechstedt, Phys. Rev. B **79**, 235114 (2009)

62. F. Aryasetiawan, O. Gunnarsson, Phys. Rev. Lett. **74**, 3221 (1995)

63. M. Cococcioni, S. De Gironcoli, Phys. Rev. B **71**, 035105 (2005)

64. X. Ren, I. Leonov, G. Keller, M. Kollar, I. Nekrasov, D. Vollhardt, Phys. Rev. B **74**, 195114 (2006)

65. F. Manghi, C. Calandra, S. Ossicini, Phys. Rev. Lett. **73**, 3129 (1994)

66. R. Eder, Phys. Rev. B **76**, 241103 (2007)

67. Q. Yin, A. Gordienko, X. Wan, S. Y. Savrasov, Phys. Rev. Lett. **100**, 066404 (2008)

68. O. Miura, T. Fujiwara, Phys. Rev. B **77**, 195124 (2008)

69. This conceptual picture was suggested to one of us (JK) by J. W. Allen.

70. H. Ishida, A. Liebsch, Phys. Rev. B **81**, 054513 (2010)

71. A. Laeuchli, P. Werner, Phys. Rev. B **80**, 235117 (2009)

72. C. S. Yoo, B. Maddox, J.-H. P. Klepeis, V. Iota, W. Evans, A. McMahan, M. Y. Hu, P. Chow, M. Somayazulu, D. Häusermann, R. T. Scalettar, W. E. Pickett, Phys. Rev. Lett. **94**, 115502 (2005)

73. A. G. Gavriliuk, V. V. Struzhkin, I. S. Lyubutin, S. G. Ovchinnikov, M. Y. Hu, P. Chow, Phys. Rev. B **77**, 155112 (2008)

74. I. S. Lyubutin, S. G. Ovchinnikov, A. G. Gavriliuk, V. V. Struzhkin, Phys. Rev. B **79**, 085125 (2009)

75. R. E. Cohen, I. I. Mazin, D. G. Isaak, Science **275**, 654 (1997)

76. C. G. Shull, W. A. Strauser, E. O. Wollan, Phys. Rev. **83**, 333 (1951)

77. A. Fujimori, M. Saeki, N. Kimizuka, M. Taniguchi, S. Suga, Phys. Rev. B **34**, 7318 (1986)

78. C.-Y. Kim, C.-Y. Kim, M. J. Bedzyk, E. J. Nelson, J. C. Woicik, L. E. Berman, Phys. Rev. B **66**, 085115 (2002)

79. R. J. Lad, V. E. Henrich, Phys. Rev. B **39**, 13478 (1989)

80. S. Mochizuki, Phys. Status Solidi A **41**, 591 (1977)

81. K.-H. Kim, S.-H. Lee, J.-S. Choi, J. Phys. Chem. Solids **46**, 331 (1985)

82. M. P. Pasternak, G. Kh. Rozenberg, G. Yu. Machavariani, O. Naaman, R. D. Taylor, R. Jeanloz, Phys. Rev. Lett. **82**, 4663 (1999)

83. G. Kh. Rozenberg, L. S. Dubrovinsky, M. P. Pasternak, O. Naaman, T. Le Bihan, R. Ahuja, Phys. Rev. B **65**, 064112 (2002)

84. H. Liu, W. A. Caldwell, L. R. Benedetti, W. Panero, R. Jeanloz, Phys. Chem. Miner. **30**, 582 (2003)

85. J. Badro, G. Fiquet, V. V. Struzhkin, M. Somayazulu, H.-K. Mao, G. Shen, T. Le Bihan, Phys. Rev. Lett. **89**, 205504 (2002)

86. Y. Noguchi, K. Kusaba, K. Fukuoka, Y. Syono, Geophys. Res. Lett. **23**, 1469 (1996)

87. Y. Mita, Y. Sakai, D. Izaki, M. Kobayashi, S. Endo, S. Mochizuki, phys. stat. sol. (b) **223**, 247 (2001)

88. Y. Mita, D. Izaki, M. Kobayashi, S. Endo, Phys. Rev. B **71**, 100101 (2005)

89. J. R. Patterson, C. M. Aracne, D. D. Jackson, V. Malba, S. T. Weir, P. A. Baker, Y. K. Vohra, Phys. Rev. B **69**, 220101 (2004)

90. C. S. Yoo, B. R. Maddox, J.-H. P. Klepeis, V. Iota, W. Evans, A. McMahan, M. Hu, P. Chow, M. Somayazulu, D. Häusermann, R. T. Scalettar, W. E. Pickett, Phys. Rev. Lett. **94**, 115502 (2005)

91. J.-P. Rueff, A. Mattila, J. Badro, G. Vankò, A. Shukla, J. Phys.: Cond. Matt. **17**, S717 (2005)

92. P. Werner, A. J. Millis, Phys. Rev. Lett. **99**, 126405 (2007)

93. W. M. Xu, O. Naaman, G. Kh. Rozenberg, M. P. Pasternak, R. D. Taylor Phys. Rev. B **64**, 094411 (2001)

94. D. J. Adams, B. Amadon, Phys. Rev. B **79**, 115114 (2009)

95. The problem of equilibrium volume of number of simple elements has been also recently addressed in I. Di Marco, J. Minár, S. Chadov, M. I. Katsnelson, H. Ebert, A. I. Lichtenstein, Phys. Rev. B **79**, 115111 (2009), and A. Kutepov, S. Y. Savrasov, G. Kotliar, Phys. Rev. B **80**, 041103 (2009).

96. H. A. Jahn, E. Teller, Proc. R. Soc. London Ser. A **161**, 220 (1937)

97. D. I. Khomskii, K. I. Kugel, Solid State Comm. **13**, 763 (1973)

98. K. I. Kugel, D. I. Khomskii, Sov. Phys. Solid State **17**, 285 (1975)

99. K. I. Kugel, D. I. Khomskii, Sov. Phys. JETP **52**, 501 (1981)

100. K. I. Kugel, D. I. Khomskii, Sov. Phys. Usp. **25**(4), 231 (1982)

101. O. K. Andersen, Phys. Rev. B **12**, 3060 (1975)

102. O. K. Andersen, T. Saha-Dasgupta, Phys. Rev. B **62**, R16219 (2000)

103. I. Leonov, N. Binggeli, Dm. Korotin, V. I. Anisimov, N. Stojić, D. Vollhardt, Phys. Rev. Lett. **101**, 096405 (2008)

104. I. Leonov, Dm. Korotin, N. Binggeli, V. I. Anisimov, D. Vollhardt, Phys. Rev. B **81**, 075109 (2010)

105. G. Trimarchi, I. Leonov, N. Binggeli, Dm. Korotin, V. I. Anisimov, J. Phys.: Condens. Matter **20**, 135227 (2008)

106. Dm. Korotin, A. V. Kozhevnikov, S. L. Skornyakov, I. Leonov, N. Binggeli, V. I. Anisimov, G. Trimarchi, Eur. Phys. J. B **65**, 91 (2008)

107. B. Amadon, F. Lechermann, A. Georges, F. Jollet, T. O. Wehling, A. I. Lichtenstein, Phys. Rev. B **77**, 205112 (2008)

108. For a formulation of LDA+DMFT within a mixed-basis pseudopotential approach see F. Lechermann, A. Georges, A. Poteryaev, S. Biermann, M. Posternak, A. Yamasaki, O. K. Andersen, Phys. Rev. B **74**, 125120 (2006)

109. To describe the thermodynamics of solids one must, in principle, also compute the entropy and consider the electronic, magnetic and lattice (vibrational) contributions in the Gibbs free energy. The first two contributions are generally small and can be neglected in the paramagnetic phase of a wide-band insulator, whereas the lattice entropy may have an influence on a structural phase transition. To estimate its contribution would require to perform molecular dynamics calculations for a correlated system. This is a very demanding project which we plan to do in the future.

110. S. Kadota, I. Yamada, S. Yoneyama, K. Hirakawa, J. Phys. Soc. Jpn. **23**, 751 (1967)

111. R. H. Buttner, E. N. Maslen, N. Spadaccini, Acta Cryst. B **46**, 131 (1990)

112. J. B. Goodenough, *Magnetism and the Chemical Bond* (Interscience, New York, 1963)

113. J. E. Medvedeva, M. A. Korotin, V. I. Anisimov, A. J. Freeman, Phys. Rev. B **65**, 172413 (2002)

114. E. Pavarini, E. Koch, A. I. Lichtenstein, Phys. Rev. Lett. **101**, 266405 (2008)

115. N. Binggeli, M. Altarelli, Phys. Rev. B **70**, 085117 (2004)

116. In general, GGA tends to give better results than LDA for the electronic and structural properties of complex oxides and related materials. See, D. R. Hamann, Phys. Rev. Lett. **76**, 660 (1996) and H. Sawada, Y. Morikawa, K. Terakura, N. Hamada, Phys. Rev. B **56**, 12154 (1997)

117. M. T. Hutchings, E. J. Samuelsen, G. Shirane, K. Hirakawa, Phys. Rev. **188**, 919 (1969)

118. T. Ueda, K. Sugawara, T. Kondo, I. Yamada, Solid State Commun. **80**, 801 (1991)

119. I. Yamada, H. Fujii, M. Hidaka, J. Phys. Condens. Matter **1**, 3397 (1989)

120. M. V. Eremin, D. V. Zakharov, H.-A. Krug von Nidda, R. M. Eremina, A. Shuvaev, A. Pimenov, P. Ghigna, J. Deisenhofer, A. Loidl, Phys. Rev. Lett. **101**, 147601 (2008)

121. J. Deisenhofer, I. Leonov, M. V. Eremin, Ch. Kant, P. Ghigna, F. Mayr, V. V. Iglamov, V. I. Anisimov, D. van der Marel, Phys. Rev. Lett. **101**, 157406 (2008)
122. L. Paolasini, R. Caciuffo, A. Sollier, P. Ghigna, M. Altarelli, Phys. Rev. Lett. **88**, 106403 (2002)
123. R. Caciuffo, L. Paolasini, A. Sollier, P. Ghigna, E. Pavarini, J. van den Brink, M. Altarelli, Phys. Rev. B **65**, 174425 (2002)
124. Calculations have been performed using the Quantum ESPRESSO package, see Ref. [10,11], http://www.quantum-espresso.org
125. The local coordinate system is chosen with the z direction defined along the longest (in ab plane) Cu-F bond of the CuF_6 octahedron.
126. Here we perform DMFT calculations for a fixed DFT Hamiltonian $\hat{H}_{DFT}$, thereby neglecting full charge self-consistency which is not expected to change the results significantly [32].
127. To simplify the computation we neglected the orbital off-diagonal elements of the local Green function by applying an additional transformation into the local basis set with a diagonal density matrix during each DMFT iteration.
128. J. B. A. A. Elemans, B. van Laar, K. R. van der Veen, B. O. Loopstra, J. Phys. Chem. Solids **3**, 238 (1971)
129. J. Rodriguez-Carvajal, M. Hennion, F. Moussa, A. H. Moudden, L. Pinsard, A. Revcolevschi, Phys. Rev. B **57**, R3189 (1998)
130. T. Chatterji, F. Fauth, B. Ouladdiaf, P. Mandal, B. Ghosh, Phys. Rev. B **68**, 052406 (2003)
131. G. Trimarchi, N. Binggeli, Phys. Rev. B **71**, 035101 (2005)
132. Th. Pruschke, M. B. Zölfl, *Advances in Solid State Physics* **40**, 251 (2000); See also R. Peters, Th. Pruschke, cond-mat/0908.3990, where the authors discuss the interplay of orbital and spin degrees of freedom in the two orbital Hubbard model near quarter filling.
133. A. Yamasaki, M. Feldbacher, Y.-F. Yang, O. K. Andersen, K. Held, Phys. Rev. Lett. **96**, 166401 (2006)
134. K. Held, O. K. Andersen, M. Feldbacher, A. Yamasaki, Y.-F. Yang, J. Phys.: Condens. Matter **20**, 064202 (2008)
135. E. Pavarini, E. Koch, cond-mat/0904.4603
136. W.-G. Yin, D. Volja, W. Ku, Phys. Rev. Lett. **96**, 116405 (2006)
137. The local coordinate system is chosen such that the GGA Mn $3d$ density matrix has a diagonal form.
138. A. J. Millis, B. I. Shraiman, R. Mueller, Phys. Rev. Lett. **77**, 175 (1996)
139. K. Held, D. Vollhardt, Phys. Rev. Lett. **84**, 5168 (2000)
140. I. A. Nekrasov, K. Held, G. Keller, D. E. Kondakov, T. Pruschke, M. Kollar, O. K. Andersen, V. I. Anisimov, D. Vollhardt, Phys. Rev. B **73**, 155112 (2006)
141. O. Gunnarsson, O. K. Andersen, O. Jepsen, J. Zaanen, Phys. Rev. B **39**, 1708 (1989)
142. K. Byczuk, M. Kollar, K. Held, Y.-F. Yang, I. A. Nekrasov, T. Pruschke, D. Vollhardt, Nature Physics **3**, 168 (2007)
143. T. Yoshida, K. Tanaka, H. Yagi, A. Ino, H. Eisaki, A. Fujimori, Z.-X. Shen, Phys. Rev. Lett. **95**, 146404 (2005)
144. M. Takizawa, M. Minohara, H. Kumigashira, D. Toyota, M. Oshima, H. Wadati, T. Yoshida, A. Fujimori, M. Lippmaa, M. Kawasaki, H. Koinuma, G. Sordi, M. Rozenberg, Phys. Rev. B **80**, 235104 (2009)
145. A. Toschi, M. Capone, C. Castellani, K. Held, Phys. Rev. Lett. **102**, 076402 (2009)
146. C. Raas, P. Grete, G. S. Uhrig, Phys. Rev. Lett. **102**, 076406 (2009)
147. A. Hofmann, X. Y. Cui, J. Schäfer, S. Meyer, P. Höpfner, C. Blumenstein, M. Paul, L. Patthey, E. Rotenberg, J. Bünemann, F. Gebhard, T. Ohm, W. Weber, R. Claessen, Phys. Rev. Lett. **102**, 187204 (2009)